Physics of Fluids

RESEARCH ARTICLE | AUGUST 05 2026

Numerical study on suppressing heat transfer deterioration of supercritical CO_2 in tube with wire-mesh inserts

Qiuru Dong (董邱儒) ; Zhen Cao (曹桢) ; Jian Xie (谢剑) ; Jinliang Xu (徐进良) ; Xin Wang (王欣); Jing Tang (唐婧)

Check for updates

Physics of Fluids 38, 083306 (2026)
https://doi.org/10.1063/5.0340149

View Online Export Citation

Articles You May Be Interested In

Thermohydraulic performance of a printed circuit heat exchanger with ribbed cross-connected semicircular channel

Physics of Fluids (February 2025)

Thermohydraulic performance of a novel curved serpentine coil

Physics of Fluids (August 2020)

The matching effect of the cold-to-hot fluid on the thermohydraulic characteristics of heat exchangers using gyroid-typed triply periodic minimal surfaces

Physics of Fluids (February 2025)

10 October 2026 07:25:36

AIP Publishing

Physics of Fluids

Special Topics Open for Submissions

Learn More

AIP Publishing

Physics of Fluids ARTICLE pubs.aip.org/aip/pof

Numerical study on suppressing heat transfer deterioration of supercritical CO_2 in tube with wire-mesh inserts

Cite as: Phys. Fluids **38**, 083306 (2026); doi: 10.1063/5.0340149
Submitted: 23 April 2026 · Accepted: 17 July 2026 ·
Published Online: 5 August 2026

View Online Export Citation CrossMark

Qiuru Dong (董邱儒),[1] Zhen Cao (曹桢),[2] Jian Xie (谢剑),[1,a)] Jinliang Xu (徐进良),[1,3] Xin Wang (王欣),[1] and Jing Tang (唐婧)[1]

AFFILIATIONS

[1]Beijing Key Laboratory of Multiphase Flow and Heat Transfer for Low Grade Energy Utilization, North China Electric Power University, Beijing 102206, China
[2]Department of Chemical Engineering, Imperial College London, London SW7 2AZ, United Kingdom
[3]Key Laboratory of Power Station Energy Transfer Conversion and System of Ministry of Education, North China Electric Power University, Beijing 102206, China

[a)]Author to whom correspondence should be addressed: xiejian90@ncepu.edu.cn

ABSTRACT

A periodic wire-mesh inserted tube is proposed to mitigate heat transfer deterioration (HTD) of supercritical carbon dioxide in upward flow through a vertical tube. Its thermohydraulic performance is numerically investigated at $p = 8$ MPa, with mass flux G ranging from 400 to 3000 kg/m^2 s and heat flux q ranging from 100 to 490 kW/m^2. The results show that effective HTD suppression is achieved only when the wire-mesh insert is arranged upstream of the deterioration region, and increasing the number of inserts enlarges the suppression region where the wall temperature is reduced. For the periodic configuration, the peak wall temperature is reduced by 91 K, maximally. It owes to enhanced near-wall fluid renewal and radial mixing, which thin the near-wall vapor-like layer and suppress thermal-boundary-layer development. Moreover, the thermohydraulic analysis indicates that the heat-transfer enhancement factor and performance evaluation criterion generally increase first and then decrease with increasing mass flux and heat flux, accompanied by local fluctuations, reaching maximum values of 1.92 and 1.42, respectively. A mass flux–heat flux diagram is further constructed to distinguish the effective HTD suppression region from the weak HTD suppression region. The present study provides physical insights and design guidance for the HTD mitigation of supercritical carbon dioxide in channels.

Published under an exclusive license by AIP Publishing. https://doi.org/10.1063/5.0340149

10 October 2026 07:25:36

I. INTRODUCTION

In recent years, the global energy sector has been moving toward low carbon emissions, high energy efficiency, and high power density. Aligned with this background, the supercritical carbon dioxide (sCO_2) Brayton cycle has attracted ever-increasing interest because it presents many merits, e.g., low compression work near the critical point, high power density, and system compactness.[1] In addition, CO_2 has a relatively low critical temperature (305.34 K) and critical pressure (7.38 MPa), which makes it easy to reach and maintain supercritical operation in engineering systems, achieving superior potentials in highly efficient energy conversion and boosting energy density. Thus, sCO_2 is being widely studied[2,3] and extensively used in many applications, such as, nuclear and solar power systems, coal-fired power plants, waste-heat recovery, heat-pump systems, printed circuit heat exchangers, and the thermal management of hypersonic vehicles.[4–12] As illustrated in Fig. 1, sCO_2 exhibits drastic variations in its thermophysical properties near the pseudocritical temperature, and this strong nonlinear characteristic usually induces heat transfer deterioration (HTD) in tubes. Under high-temperature and high-pressure sCO_2 conditions, the onset of HTD typically manifests as a rise in wall temperatures and temperature gradients across the wall, which in turn increase thermal stress and elastic strain, threatening the structural integrity of tubes.[13,14] For many industrial applications, it is considerably important to understand HTD and propose suppression strategies.[15]

Supercritical fluids are typically treated as single-phase fluids in classical heat transfer. The buoyancy effect and flow acceleration effect are regarded as the primary mechanisms of HTD.[16–21] However,

Published under an exclusive license by AIP Publishing

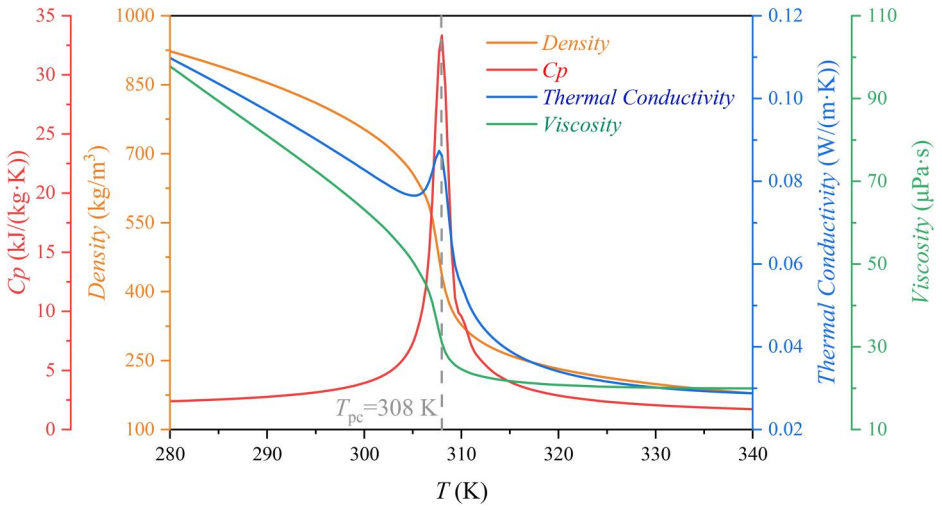


FIG. 1. Variations of CO_2 thermophysical properties at 8 MPa.

Zhu *et al.*[22] found that such dimensionless numbers were not able to well predict the occurrence of HTD in supercritical flows, based on the comprehensive analysis of experimental data in the literature. This indicates that treating supercritical fluids as single phase has its limitations to understand the mechanism of HTD occurrence. In contrast, molecular dynamics simulations, experimental observations, and theoretical analyses show that the supercritical fluid presents multiphase-like features in near-critical conditions.[23–28] Wang *et al.*[29] proposed that the supercritical liquid has three phases: liquid-like (LL), vapor-like (VL), and a transitional pseudo-two-phase-like (TPL) phase. During continuous heating, the supercritical liquid evolves from LL to VL, similar to boiling in subcritical conditions, called pseudo-boiling.[30] Zhu *et al.*[31] defined normal heat transfer (NHT) with temperature-overshoot $\Delta T < 8$ K and heat transfer deterioration (HTD) with $\Delta T > 8$ K. They further developed pseudo-boiling theory, and the supercritical boiling number (*SBO*) was proposed as a new dimensionless number. It was found that *SBO* had critical values to distinguish NHT and HTD well, highlighting the validation to treat the supercritical fluid as multiphase flow.

In recent years, the role of the near-wall vapor-like/gas-like layer in abnormal heat transfer of supercritical CO_2 has received increasing attention. Cheng and Xu performs heat transfer experiment of supercritical CO_2 and attributes the onset of HTD and wall-temperature overshoot to the increasing vapor-like layer thickness.[32] Yu *et al.* confirm that the change trend of vapor-like layer thickness matches with that of wall-temperature overshoot along the flow direction in HTD cases.[33] More recently, Dolatabadi *et al.* systematically investigated the relationship between gas-like layer and the onset of HTD under various boundary conditions. A new correlation incorporating the pseudo-mass quality was developed to account for the gas-like layer. It demonstrates about 94% accuracy on predicting the onset of HTD.[34] These studies suggest that enhancing near-wall mixing and suppressing the continuous development of the vapor-like layer are effective ways to alleviate HTD. In summary, more and more research supports the perspective that the supercritical fluids feature multiphase characteristics and the supercritical heat transfer features a pseudo-boiling process. Therefore, heat transfer could be modulated by changing the multiphase behavior (e.g., vapor-like thickness) during pseudo-boiling.

There are mainly two well-established passive methods to suppress HTD in supercritical CO_2 flow. The first one is to promote fluid mixing by secondary flow introduced in curved/swirled channels. For example, vertical serpentine tubes exploit periodic curvature variations to induce centrifugal secondary flows, which improves fluid mixing and can prevent local HTD under conditions where buoyancy effects are pronounced.[35] Helical tubes work in a similar manner where the secondary flow driven by centrifugal forces reshapes the velocity and temperature fields, altering convective heat transfer behavior in the vicinity of the pseudocritical region.[36] The second route is to employ built-in inserts or wall structures that directly act on the near-wall region, weakening the wall-adjacent low-density layer and intensifying turbulence. For instance, a helical wire insert can induce swirling motion and thereby suppress heat transfer deterioration in a vertical tube.[37] Discrete double-inclined ribs periodically interrupt the development of the near-wall buoyancy-driven flow region and generate streamwise vortices, thereby enhancing heat transfer and reducing the peak wall temperature.[38] Dimpled surfaces, by contrast, create local vortices through flow separation and reattachment, strengthening near-wall disturbance and thus weakening or delaying HTD.[39] In addition, three-dimensional lattices or porous arrays have also been employed to enhance radial mixing and alleviate HTD, because they can produce strong disturbance and complex vortex structures across the entire cross section.[40,41] It should be noted, however, that most of these approaches have been validated only within relatively limited ranges of mass flux and heat flux. Systematic assessments remain scarce regarding their suppression capacity and pressure-drop penalty in high mass flux and high heat flux conditions.

From an engineering perspective, enhancing heat transfer is always a key issue. Previous studies have shown that wire-mesh-based structures can be fabricated, assembled, and actually used to enhance the subcritical single-phase heat transfer and condensation heat transfer. Xing *et al.* experimentally investigated a modulated heat transfer tube with a mesh-cylinder insert,[42] while Cao *et al.* further analyzed

10 October 2026 07:25:36

Published under an exclusive license by AIP Publishing

its micro–macro flow-coupling mechanism.[43] Kurian *et al.* fabricated and tested a near-compact wire-mesh heat exchanger using commercially available stainless-steel wire meshes, demonstrating the feasibility of wire-mesh structures in heat-exchanger construction.[44] In addition, Li *et al.* applied mesh-membrane-tube to suppress flooding in condenser tubes, indicating the potential engineering applicability of such wire-mesh membrane structures.[45] Xie *et al.* further provided a detailed installation method for mesh-membrane-tube inside a tube, in which short mesh-membrane-tube sections were suspended in the tube and positioned by welded connections, inlet grooves, and supporting structures to maintain a uniform gap.[46] These studies indicate that wire-mesh-based structures can effectively modulate the heat transfer in tubes. Motivated by this, the present paper further explores the role of wire-mesh inserts in modulating sCO_2 heat transfer. It focuses on the mechanisms of HTD suppression under high mass flux and high heat flux conditions.

Numerical simulation has been widely used for the mechanism analysis of supercritical CO_2 heat transfer deterioration and the preliminary evaluation of its mitigation strategies.[35–41] Compared with experimental measurements, numerical methods can provide more detailed local flow field, temperature field, and phase distribution. This information is important to reveal the underlying mechanism of insert structures to suppress HTD. In this study, the periodic wire-mesh inserted tube (PWMIT) is considered as a potential HTD mitigation structure. Its effects on peak wall temperature, heat transfer capacity, and pressure drop are investigated numerically. It should be noted that the present work is mainly positioned as a mechanism-oriented numerical study, and further experimental validation and structural reliability assessment are still required in future work.

II. MATHEMATICAL MODEL AND CALCULATION METHOD

A. Geometric model

Figure 2(a) shows the geometry of the heat transfer tube, which has an inner diameter $D = 10$ mm, consistent with that used in our previous experimental measurements.[31] The computational domain consists of an inlet adiabatic section (600 mm in length), a heated section (2000 mm in length), and an outlet adiabatic section (600 mm in length). The inlet section ensures that the working fluid is fully developed before entering the heated region, while the outlet section guarantees that the supercritical flow is steady at the end of the heated section. Figure 2(b) shows a periodic wire-mesh inserted tube (PWMIT) in which wire-mesh cylinders are arranged at an interval $L_b = 200$ mm along the tube's centerline, dividing the cross section into an outer annular region and an inner core region. The wire-mesh cylinder has a mesh layer on the top and side, with a hollow interior. This configuration produces high velocity and velocity gradient in the annular region near the wall, thereby enhancing local heat transfer.

B. Model conversion from 3D to 2D

This PWMIT involves the micrometer-scale length of the mesh openings, the millimeter-scale length of the annular flow passage, and the meter-scale length of the entire tube, thus exhibiting pronounced multi-scale characteristics. Figure 2(c) shows the three-dimensional wire-mesh cylinder, with its diameter and height, $D_m = 7$ mm and $L_m = 50$ mm, respectively, while the square opening width and wire diameter are denoted by w and δ. When 10 wire-mesh inserts are installed in the tube with $w = 165\,\mu$m and $\delta = 85\,\mu$m, the three-dimensional model contains $\sim 1.75 \times 10^5$ mesh openings, which pose extreme challenges in geometry construction and mesh generation as well as simulations. More importantly, the coexistence of micro and macro structures in such a configuration makes it difficult for conventional modeling approaches to simultaneously capture the flow and heat transfer behavior.

Therefore, to reduce the computational burden while maintaining practical feasibility, the original geometry must be appropriately simplified through geometric reduction and scale transformation. Although the internal structure of the heated tube is relatively complex, the key flow and heat transfer effects mainly arise from the local disturbance induced by the wire mesh. Thus, the dominant physics can be captured by constructing a computationally affordable two-dimensional (2D) model through an equivalent simplification of the three-dimensional (3D) wire-mesh geometry. Converting the 3D mesh cylinder into a 2D structure not only enables effective simulation of flow and heat transfer with much lower computational cost, but also reproduces the key features of flow and heat transfer. Such simplification has been validated in Ref. 43. Specifically, by converting the square openings in Fig. 2(c) with the slotted openings shown in Fig. 2(d), the simulation domain can be simplified as a two-dimensional domain, where the slot width and wire thickness in the 2D model are denoted by w' and δ', respectively. The 3D-to-2D transformation method follows the method proposed in Ref. 43.

1. Equivalent hydraulic diameter consistency

When simplifying the three-dimensional wire-mesh geometry into a two-dimensional model, the first step is to ensure that the two models are consistent in terms of the pore's equivalent (hydraulic) size. For the square pore in the 3D mesh shown in Fig. 2(c), the equivalent diameter can be obtained as

$$D_e = 4\frac{w^2}{4w} = w. \tag{1}$$

As shown in Fig. 2(d), the 2D model employs a slit-type pore which has an equivalent hydraulic diameter as

$$D'_e = 4\frac{w' D_m}{2D_m} = 2w'. \tag{2}$$

By equating the hydraulic diameters of the 3D and 2D models, i.e., $D_e = D'_e$, it is obtained that $w' = 0.5\,w$.

2. Flow-area consistency

During the 3D-to-2D conversion, it is also necessary to preserve the flow-passage area. For the 3D wire-mesh structure in Fig. 2(c), the total flow area can be expressed as

$$A = \frac{\pi D_m}{w+\delta} \times \frac{L_m}{w+\delta} \times w^2, \tag{3}$$

where $\pi D_m/(w + \delta)$ and $L_m/(w + \delta)$ represent the number of pores along the circumferential direction and the axial direction, respectively. For the 2D slit-type pores in Fig. 2(d), the flow area is

10 October 2026 07:25:36

Published under an exclusive license by AIP Publishing

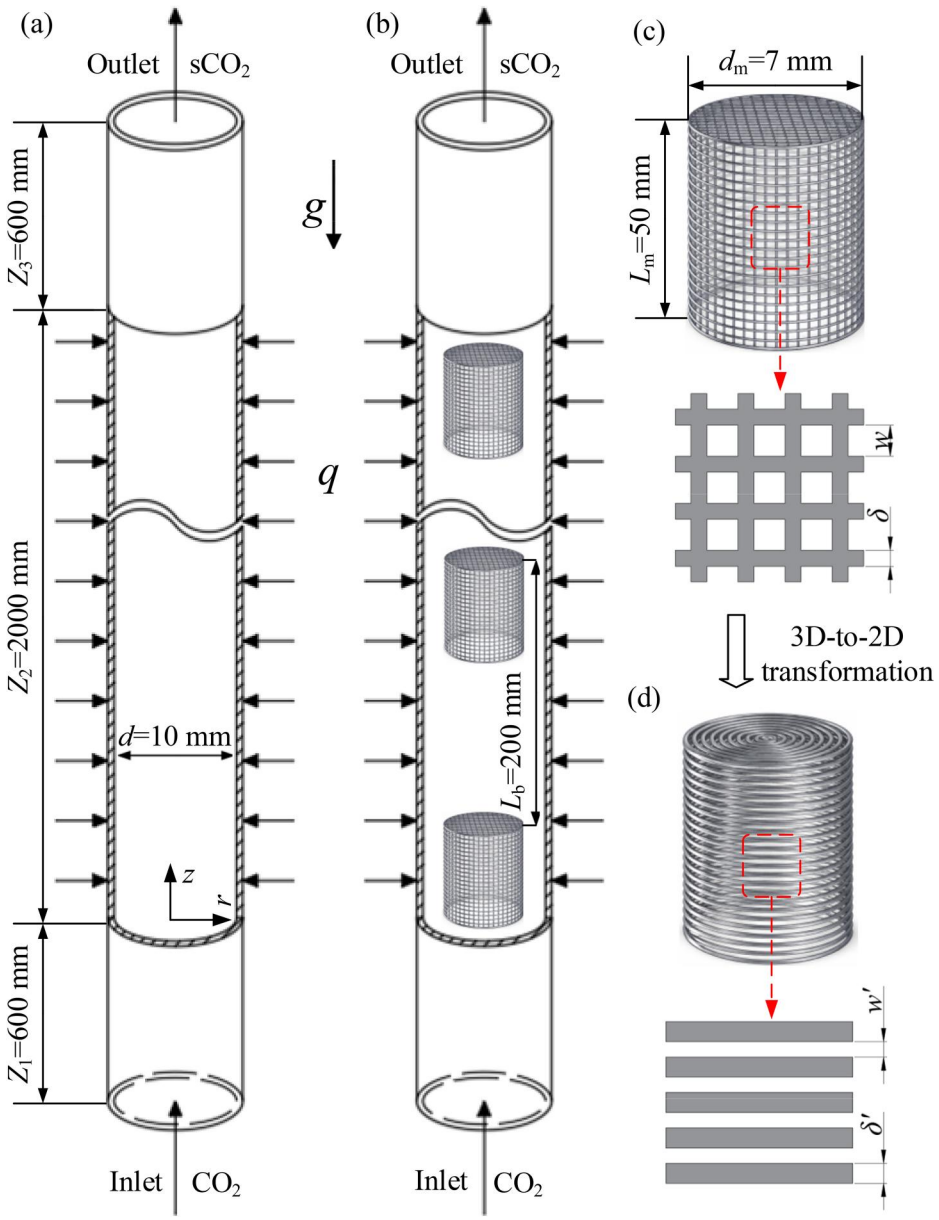


FIG. 2. Computational domain and 3D-to-2D equivalent transformation of the wire-mesh structure: (a) bare tube (BT); (b) tube with wire-mesh inserts; (c) 3D cylindrical unit of a square-aperture wire mesh; and (d) equivalent representation of the 3D mesh unit as a 2D strip-aperture geometry (3D-to-2D transformation).

$$A' = \frac{L_m}{w' + \delta'} \times \pi D_m w'. \tag{4}$$

To have the flow area consistent, i.e., $A = A'$, we obtain

$$\delta' = \delta + \frac{\delta^2}{2w}. \tag{5}$$

For pores per inch $PPI = 100$, the corresponding three-dimensional wire-mesh geometrical parameters are $w = 165\ \mu$m and $\delta = 85\ \mu$m. After the 3D-to-2D equivalent conversion, the slit width and equivalent wire diameter in the two-dimensional model are $w' = 82.5\ \mu$m and $\delta' = 107\ \mu$m, respectively.

C. Numerical models

The Reynolds-averaged Navier–Stokes (RANS) method is adopted in the present study mainly to obtain the averaged flow and heat transfer characteristics under steady-state operating conditions. Existing experimental studies have shown that, after a supercritical fluid heat transfer system in a tube reaches a steady state, monitored parameters such as wall temperature and pressure drop fluctuate only slightly with time; therefore, time-averaged thermal-hydraulic parameters can be used to characterize the corresponding operating condition.[27] Meanwhile, supercritical pseudo-boiling differs from subcritical boiling, in which vigorous bubble dynamics and vapor–liquid interface evolution occur. Instead, it is more similar to an

10 October 2026 07:25:36

Published under an exclusive license by AIP Publishing

evaporation process, with a relatively stable interface variation.[47] Therefore, it is reasonable to use the RANS method to analyze its time-averaged flow and heat transfer characteristics. The present study focuses on the effects of wire-mesh inserts on averaged heat transfer, HTD suppression, and pressure-drop penalty, rather than transient interface tracking. More refined volume-of-fluid (VOF)-type interface tracking would require the development of new numerical methods.[48]

In this study, turbulent flow and heat transfer of supercritical CO_2 is simulated in a vertical tube. Previous studies have shown that the shear-stress transport (SST) k–ω model is suitable for the simulation of supercritical flow and heat transfer.[49–52] The model uses the k–ω formulation in the near-wall region and blends it toward a k–ε-type behavior in the outer flow, improving robustness and the prediction of turbulent viscosity.[53] Thus, the present work also employs the SST k–ω model. The governing equations are show as below, including mass conservation equations, momentum equations, and energy equations:

$$\frac{\partial \rho}{\partial t} + \frac{\partial (\rho u_i)}{\partial x_i} = 0, \tag{6}$$

$$\frac{\partial (\rho u_i)}{\partial t} + \frac{\partial (\rho u_i u_j)}{\partial x_j} = -\frac{\partial p}{\partial x_i} + \frac{\partial}{\partial x_j}\left[\mu\left(\frac{\partial u_i}{\partial x_j} + \frac{\partial u_j}{\partial x_i}\right)\right] + \frac{\partial}{\partial x_j}\left[-\rho \overline{u_i' u_j'}\right] + \rho g_i, \tag{7}$$

$$\frac{\partial (\rho h)}{\partial t} + \frac{\partial (\rho u_i h)}{\partial x_i} = \frac{\partial}{\partial x_i}\left[\left(\lambda + \frac{\mu_t c_p}{Pr_t}\right)\frac{\partial T}{\partial x_i}\right], \tag{8}$$

where $-\rho \overline{u_i' u_j'}$ denotes the Reynolds-stress term and g_i is the gravitational acceleration component. μ_t is the turbulent viscosity and Pr_t is the turbulent Prandtl number. Thermophysical properties are treated as functions of temperature and pressure to capture the strong variations near the pseudocritical region.

The SST k–ω model solves the transport equations for the turbulent kinetic energy k and the specific dissipation rate ω,

$$\frac{\partial (\rho k)}{\partial t} + \frac{\partial (\rho u_j k)}{\partial x_j} = P_k - \beta^* \rho k \omega + \frac{\partial}{\partial x_j}\left[(\mu + \sigma_k \mu_t)\frac{\partial k}{\partial x_j}\right], \tag{9}$$

$$\frac{\partial (\rho \omega)}{\partial t} + \frac{\partial (\rho u_j \omega)}{\partial x_j} = \gamma \frac{\omega}{k} P_k - \beta \rho \omega^2 + \frac{\partial}{\partial x_j}\left[(\mu + \sigma_\omega \mu_t)\frac{\partial \omega}{\partial x_j}\right] + D_\omega, \tag{10}$$

where P_k is the production term of turbulent kinetic energy, and D_ω is the cross-diffusion term that enables a smooth transition between the near-wall k–ω behavior and the outer-flow formulation. The remaining variables, model constants, and blending functions follow the standard SST k–ω formulation and further details can be found in Ref. 51.

D. Mesh generation and solution strategy

The wire-mesh inserted tube presents multiscale characteristics, with micro-scale mesh pores and millimeter-scale in tube diameter and meter-scale in tube length. To convincingly capture critical physical features in the tube with affordable number of meshes, multi-scale meshes were generated, meaning that different scale of meshes were adopted in different regions. Micro-scale meshes were used in the wire-mesh pores, which are gradually enlarged to millimeter-scale meshes in the bulk region. Figure 3 shows the grid system. Here, $PPI = 100$ is taken as an example to describe the mesh-generation strategy. In general, quadrilateral structured meshes were generated, with local refinement in different regions. Approximately, uniform meshes were used in the bulk flow region away from the wire mesh, with a typical cell size of 94.75 μm. Owing to the large velocity and temperature gradients near the wire-mesh surface, the near-wall meshes were refined with a first-layer thickness of 2.59 μm and expanding outward with a growth ratio of 1.1. Refined structured meshes with a cell size of $18.95 \times 18.95\ \mu m^2$ were applied in the vicinity of the wire mesh, and a smooth transition to both the ultra-fine near-wall mesh and the base mesh in the bulk region was achieved through multiple layers of quadrilateral cells, maintaining mesh quality and numerical stability in the local region.

In terms of the mesh nearby the tube wall, the distance from the wall to the first node in the fluid domain was set to 1.5 μm, and a boundary-layer mesh was generated using the same radial growth ratio of 1.1, ensuring that the dimensionless wall distance y^+ remained below 1 throughout the calculation. For the simulation domain with ten wire-mesh inserts, the total number of cells was 4.93×10^6.

Based on the above mesh system, the governing equations for flow and heat transfer were solved using the computational fluid dynamics software ANSYS Fluent 19.2,[54] while geometry construction and mesh generation were completed in Gambit. The inlet and outlet of the computational domain were defined as mass-flow-inlet and pressure-outlet boundaries, respectively. A constant heat flux and adiabatic conditions were applied to the heated and adiabatic sections of the tube wall, respectively. The numerical solution employed an implicit algorithm based on pressure–velocity coupling, in which the coupled method was used for pressure correction in the momentum equations. The pressure term was discretized using the standard scheme, while both the momentum and energy equations were solved using second-order upwind discretization. The relaxation factors for all equations were set in the range of 0.2–0.8. To accurately account for the drastic variations in the thermophysical properties of supercritical CO_2 with temperature and pressure, fluid properties were queried from the National Institute of Standards and Technology (NIST) real-gas database and imported into Fluent using a piecewise-linear approach. In the simulation, the operating pressure and inlet temperature were set to 8 MPa and 298 K, respectively. The residual convergence criteria for the continuity and momentum equations were set as 10^{-4}, while the criterion for the energy equation was set as 10^{-7}. The computation was considered converged when the residuals of all equations satisfied the requirements, and the temperature and pressure at the outlet became stable.

E. Grid independence test for the bare tube

To ensure the reliability of the numerical results, a grid independence test was performed. Two representative operating conditions were selected, namely, a normal heat transfer (NHT) condition [$p = 8.221$ MPa, $G = 1\,252.3\ kg/(m^2 s)$, and $q = 244.3\ kW/m^2$] and a heat transfer deterioration (HTD) condition [$p = 8.221$ MPa, $G = 1\,001.5\ kg/(m^2 s)$, and $q = 244.3\ kW/m^2$]. The axial distributions

10 October 2026 07:25:36

Published under an exclusive license by AIP Publishing

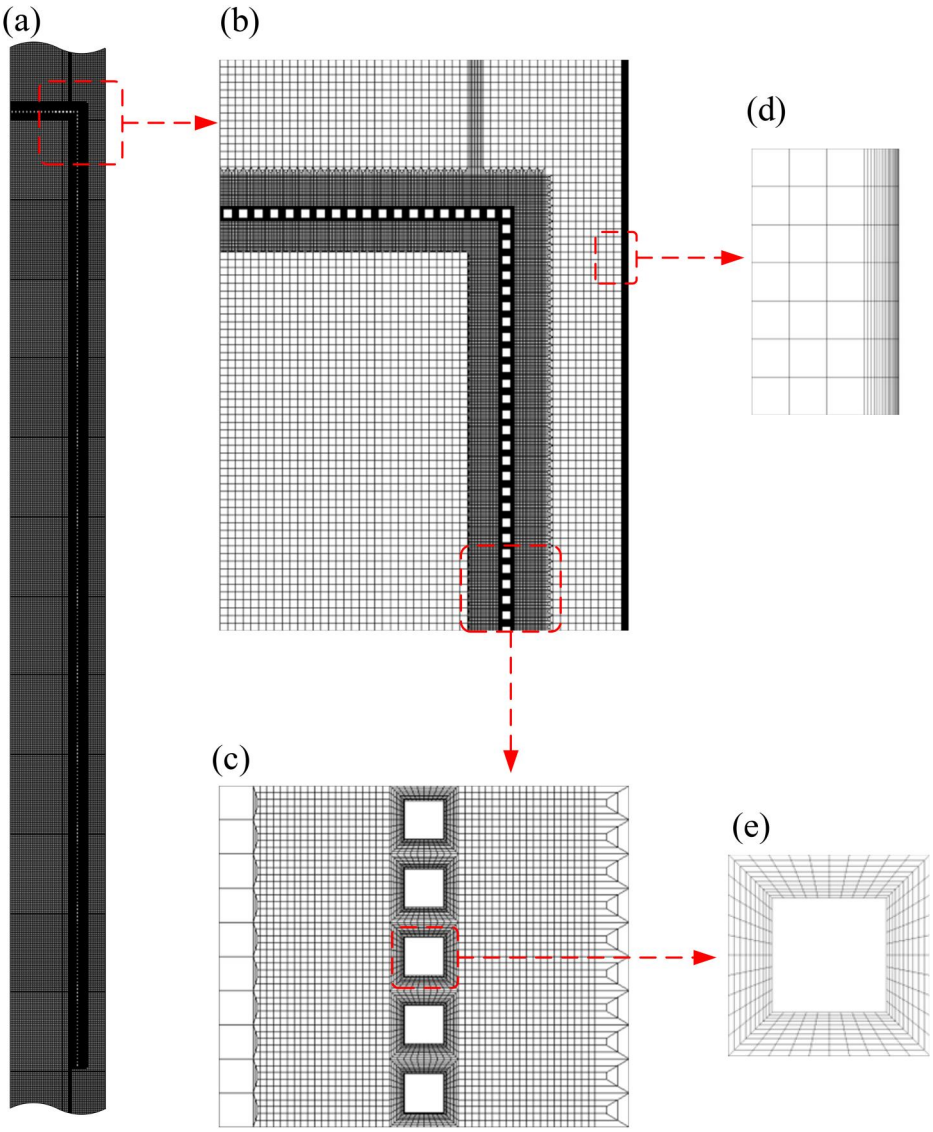


FIG. 3. Computational mesh and local refinement details: (a) mesh distribution in a representative axial segment; (b) near-wall boundary-layer refinement and mesh transition around the corner; (c) local refinement and transition near a representative wire-mesh unit; (d) close-up view of the near-wall boundary-layer mesh; and (e) refined mesh details at the corner of a square aperture.

of the inner wall temperature, T_{wi}, were compared using five grid systems of 0.72×10^6, 1.13×10^6, 1.43×10^6, 1.83×10^6, and 2.17×10^6 cells.

As illustrated in Fig. 4, in the NHT condition, the inner wall temperature T_{wi} changes very slightly in the five grid systems. In the HTD condition, it is seen that the inner wall temperature depends on the number of meshes, especially when the number of meshes is less than 1.43×10^6. The temperature differs slightly when the number of meshes is 1.83×10^6 and 2.17×10^6. Considering both accuracy and computational cost, the mesh with 1.83×10^6 cells was adopted in the present simulations.

F. Model validation

To validate the numerical model, experimental data from Ref. 31 were used for comparison. The numerical and experimental results were compared both in the NHT condition and in the HTD condition, in terms of the inner wall temperature and heat transfer coefficient. As shown in Figs. 5(a) and 5(b), the numerical result of the inner wall temperature agrees well with the measurement. The model could well capture the heat transfer deterioration characterized by an abnormal rise in the wall temperature. Quantitatively, the difference between the simulation and experiment has a mean error, e_A, of 0.966% and 3.603% in the NHT condition and HTD condition, respectively, and a standard deviation error, e_S, of 1.360% and 1.611%, respectively, demonstrating good accuracy in predicting the wall temperature.

As shown in Figs. 5(c) and 5(d), the numerical results also agree well with the experimental results concerning the heat transfer coefficient h. Compared with the discrepancy of wall temperatures, heat transfer coefficient h has a little higher difference between simulations

10 October 2026 07:25:36

Published under an exclusive license by AIP Publishing

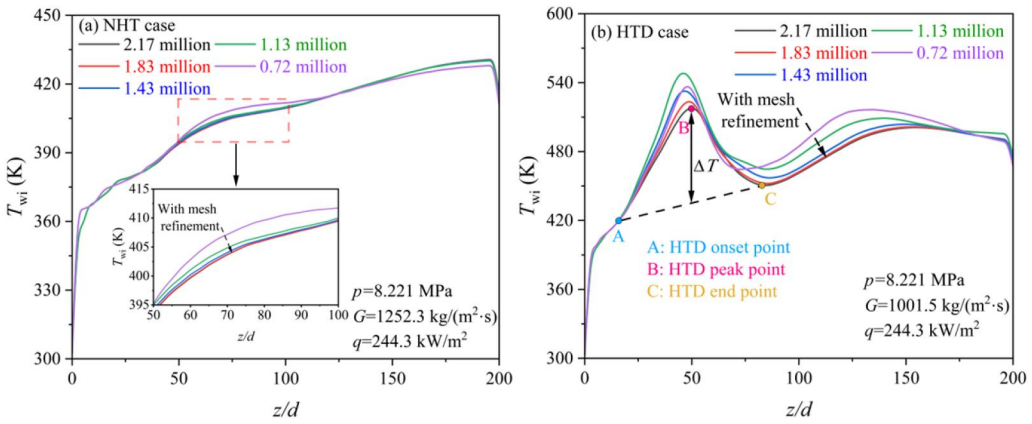


FIG. 4. Grid-independence verification: axial distributions of the inner-wall temperature, T_{wi}, as a function of z/d for different mesh sizes. (a) NHT condition and (b) HTD condition.

and experiments, particularly in the inlet region and near the local minimum under the HTD condition. The corresponding mean error, e_A, of h is 8.203% and 13.174%, respectively, while the standard deviation error, e_S, is 4.693% and 12.817%, respectively. Overall, the present model can reasonably accurately reveal the heat transfer behavior of sCO_2 under both NHT and HTD conditions and is therefore suitable for subsequent numerical investigation of heat transfer enhancement and HTD suppression mechanisms using the wire-mesh inserts.

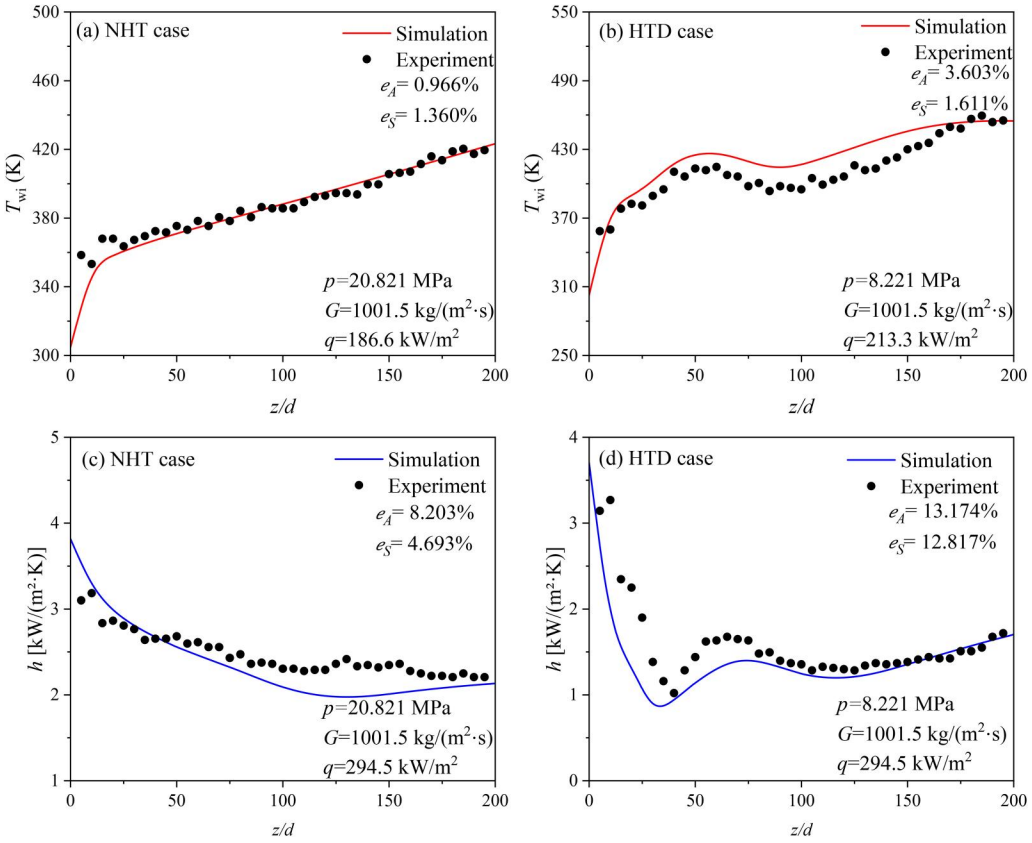


FIG. 5. Model validation by comparing the present numerical result with experimental data from Ref. 31. (a) Axial distribution of the inner-wall temperature, T_{wi}, under the NHT condition; (b) axial distribution of T_{wi} under the HTD condition; (c) axial distribution of the heat transfer coefficient, h, under the NHT condition; and (d) axial distribution of h under the HTD condition.

10 October 2026 07:25:36

Published under an exclusive license by AIP Publishing

G. Numerical treatment and model reliability analysis of the wire-mesh insert

Since the present study focuses on the flow and heat transfer of supercritical CO_2 in a tube with wire-mesh inserts, the numerical treatment of the wire-mesh structure directly affects the prediction of local flow disturbance, near-wall mixing, heat transfer enhancement, and pressure drop. Therefore, this section discusses the selection of the turbulence model, the mesh-independence analysis around the wire-mesh region, the sensitivity analysis of the turbulent Prandtl number, and the applicable scope of the model.

Regarding the turbulence model, previous numerical studies on supercritical CO_2 heat transfer in tubes with internal inserts have widely adopted the SST k–ω model as the baseline turbulence model.[38–40] The basic characteristics of the SST k–ω model and its capability for near-wall prediction have been introduced in Sec. II C. It should be further noted that the SST k–ω model generally has good applicability in predicting near-wall velocity gradients, shear stress, and local separated flows, making it suitable for the present tube-flow problem involving strong near-wall disturbance, local acceleration, and reattachment induced by the wire-mesh insert. Therefore, the SST k–ω model is adopted as the baseline turbulence model for the simulations of the wire-mesh inserted tube. It should also be clarified that the purpose of using the RANS model in this study is not to fully resolve the instantaneous vortical structures behind the wire mesh or the local anisotropic turbulent heat fluxes, but to obtain statistically averaged thermal-hydraulic characteristics, including wall temperature, heat transfer coefficient, pressure drop, and pseudo-boiling-region distribution, at an acceptable computational cost. These results are then used to analyze the HTD suppression mechanism and the overall thermal-hydraulic performance of the wire-mesh insert. More detailed transient vortical structures and turbulent heat-diffusion processes still require further investigation using large eddy simulation (LES) or direct numerical simulation (DNS).

Based on the above baseline model, a mesh-independence analysis is further conducted for the wire-mesh region. Four PWMIT models with different mesh numbers are compared, namely, 2.91×10^6, 3.75×10^6, 4.93×10^6, and 5.58×10^6 cells. The operating condition is $p = 8$ MPa, $G = 1000\ \mathrm{kg/m^2\,s}$, and $q = 180\ \mathrm{kW/m^2}$. The results are shown in Fig. 6. As the mesh is refined, the axial wall-temperature distribution gradually converges. The result obtained with 2.91×10^6 cells shows a noticeable deviation from the other three cases, especially near the locally refined region, where the wall temperature is overpredicted. In contrast, the results obtained with 3.75×10^6, 4.93×10^6, and 5.58×10^6 cells are much closer. A further comparison shows that the wall-temperature distributions for 4.93×10^6 and 5.58×10^6 cells almost overlap, indicating that further mesh refinement has only a minor influence on the main results. Therefore, considering both computational accuracy and computational cost, the mesh with 4.93×10^6 cells is adopted as the baseline mesh for the subsequent simulations.

The turbulent Prandtl number Pr_t characterizes the relative strength of turbulent momentum diffusivity and turbulent thermal diffusivity and is an important parameter in the RANS turbulence models.[55] Dolatabadi *et al.* summarized existing modified turbulent Pr_t models and showed that the selection of Pr_t is different for various fluids and flow direction.[55] For supercritical CO_2 heat transfer in upward flow through a vertical tube, Pr_t can commonly be treated as a constant value, such as 0.85 or 0.9.[56,57] Here, we conduct a sensitivity analysis of the fixed turbulent Pr_t assumption to evaluate its influence on the numerical results and main conclusions of this study. $Pr_t = 0.85$ is selected as the baseline value. Additional simulations with $Pr_t = 0.8$ and $Pr_t = 0.9$ are further conducted for comparison.

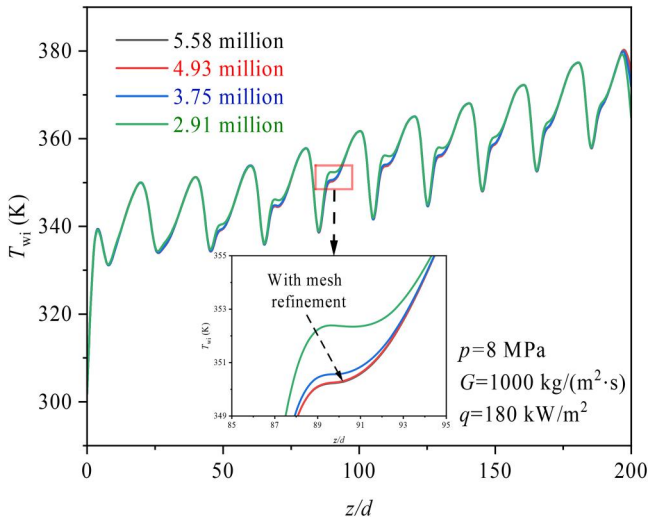


FIG. 6. Grid independence test for the periodic wire-mesh inserted tube model.

The operating condition is $p = 8$ MPa, $G = 1000\ \mathrm{kg/m^2\,s}$, and $q = 180\ \mathrm{kW/m^2}$. The numerical results for the PWMIT case under the three different turbulent Prandtl numbers are shown in Fig. 7. As shown in Fig. 7(a), the axial variations of wall temperature T_w under different Pr_t values are generally consistent. As Pr_t increases, the wall temperature slightly increases. Quantitatively, however, the influence of Pr_t on wall-temperature prediction is limited. Taking $Pr_t = 0.85$ as the baseline, the average relative errors of wall temperature for $Pr_t = 0.8$ and $Pr_t = 0.9$ are 1.04% and 1.13%, respectively, while the corresponding standard deviations of the relative errors are 0.34% and 0.35%. This indicates that within the range of $Pr_t = 0.8$–0.9, the wall temperature changes only slightly, and the axial error distribution remains relatively stable. Meanwhile, the bulk-temperature T_b curves and pressure curves corresponding to different Pr_t values in Figs. 7(a) and 7(b) almost overlap, indicating that the variation of Pr_t has little influence on the cross-sectional average temperature and pressure distribution.

In summary, as an important parameter for turbulent heat-diffusion closure, the sensitivity analysis of Pr_t is necessary. However, within the investigated range of $Pr_t = 0.8$–0.9, the overall trends of wall temperature, bulk temperature, and pressure distribution remain consistent. The average relative error of wall temperature is ~1%, and the pressure-drop results are almost unaffected. This indicates that the main conclusions of this study regarding heat transfer enhancement and flow-resistance variation induced by the wire-mesh insert do not depend on a single prescribed Pr_t value. Based on the sensitivity analysis results, and considering that $Pr_t = 0.85$ is widely adopted in engineering simulations of turbulent heat transfer, $Pr_t = 0.85$ is selected as the turbulent Prandtl number for the subsequent calculations.

10 October 2026 07:25:36

Published under an exclusive license by AIP Publishing

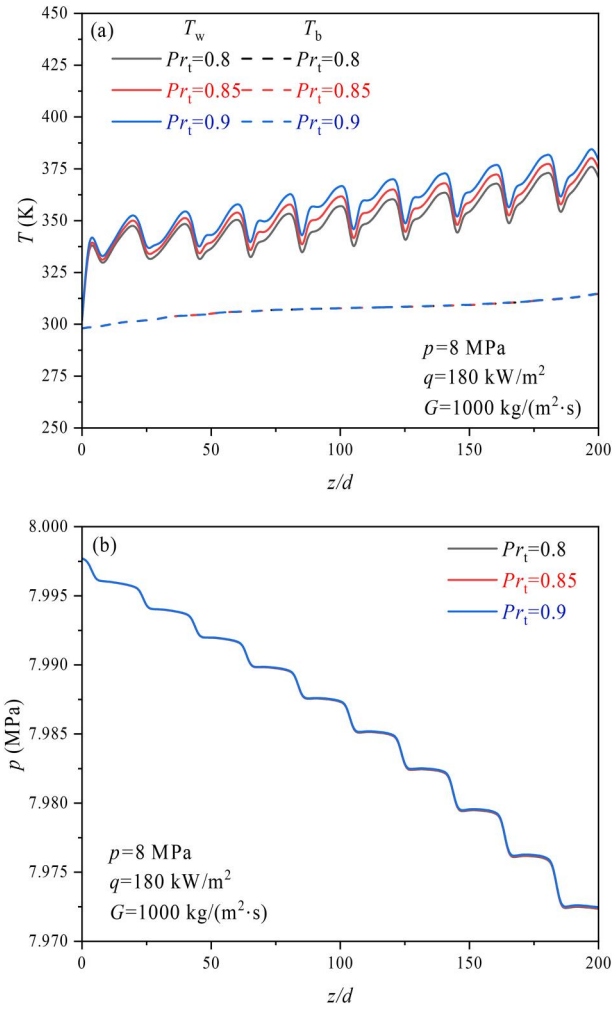


FIG. 7. Sensitivity analysis of temperature and pressure distributions in the PWMIT under different turbulent Prandtl numbers Pr_t. (a) Axial distributions of wall temperature T_w and bulk temperature T_b and (b) axial pressure distribution.

H. Selection of the baseline wire-mesh pores per inch (PPI)

The present study is a preliminary numerical exploration of HTD suppression in supercritical CO_2 tube flow, and further experimental and engineering validation will be carried out in future work. Therefore, the wire-mesh parameters were selected by considering both thermal-hydraulic performance and the feasibility of subsequent experimental fabrication. Based on our previous research experience, commercially available metal wire meshes that are mature and easy to purchase and process were used as references.

To determine the baseline pores per inch (*PPI*) for the following simulations, wire meshes with different *PPI* values were compared. Table I lists the original geometrical parameters, the equivalent two-dimensional parameters, and the corresponding peak wall temperature and pressure drop under the same operating condition. The results show that $PPI = 80$ leads to insufficient HTD suppression, while $PPI = 100$ significantly reduces the peak wall temperature from 587.39 to 397.41 K. Further increasing *PPI* to 120 only slightly reduces the peak wall temperature to 394.28 K, but causes a higher pressure drop. $PPI = 200$ does not show better HTD suppression performance.

TABLE I. The effects of wire mesh PPI on peak wall temperature and pressure drop [$p = 8$ MPa, $G = 800$ kg/(m^2 s), $q = 160$ kW/m^2].

PPI	w (μm)	δ (μm)	w' (μm)	δ' (μm)	$T_{w,max}$ (K)	Δp (Pa)
80	206	106	103	133	587.39	16 370.47
100	165	85	82.5	107	397.41	17 627.99
120	138	71	69	89	394.28	18 189.83
200	83	43	41.5	54	398.20	17 561.53

Considering the wall-temperature reduction, pressure-drop penalty, and experimental feasibility, $PPI = 100$ provides a good balance between HTD suppression and flow resistance. Therefore, $PPI = 100$ is selected as the baseline wire-mesh *PPI* for the subsequent simulations and experimental design.

III. RESULTS AND DISCUSSION

A. Effect of the position of a single wire-mesh insert on HTD suppression

To examine the effect of insert location on the suppression of HTD, a single wire-mesh insert (1 × WMI) was placed at three positions of HTD in a bare tube (BT) under the condition of $G = 1000$ kg/(m^2 s) and $q = 210$ kW/m^2: before the onset of HTD (top of the insert at $z/d = 20$), near the wall temperature peak ($z/d = 53$), and near the end of HTD ($z/d = 77$). The left side of Fig. 8 shows the axial distributions of the inner wall temperature, T_w, and the right side presents the corresponding pseudo-boiling phase diagrams. It should be noted that the pseudo-boiling phase diagrams in this study are regime maps obtained by post-processing the converged temperature field using the pseudo-boiling onset temperature T^- and termination temperature T^+. According to the pseudo-boiling theory, when the local temperature is lower than T^-, the region is identified as liquid-like; when the local temperature lies between T^- and T^+, the region is identified as two-phase-like; and when the local temperature is higher than T^+, the region is identified as vapor-like. Similar treatments have been adopted in studies of supercritical CO_2 heat transfer. Following the method in Ref. 33, at $p = 8$ MPa, $T^- = 306.5$ K and $T^+ = 310.4$ K. From the perspective of pseudo-boiling,[33] the thickness of the near-wall VL layer is a key parameter governing heat transfer performance near the pseudocritical region. Once the VL layer develops and becomes thick, the near-wall thermal resistance increases, which leads to a decline in heat transfer capacity and an overshoot in wall temperature, triggering HTD.

As shown in Fig. 8(a), the bare tube (BT) exhibits typical HTD behavior from point A to point C. The wall temperature rapidly rises near point A, and reaches the peak at point B. Then it gradually decreases to point C where the HTD ends. The peak wall temperature reaches 487 K. The position of the insert in the tube markedly affects wall temperature. It is found that the insert works the best to suppress HTD (point A to point C) when it is placed before the point A ($z/d = 20$) where HTD starts [see Fig. 8(c)]. However, there still exists a HTD region after the point B, meaning that the HTD region

10 October 2026 07:25:36

Published under an exclusive license by AIP Publishing

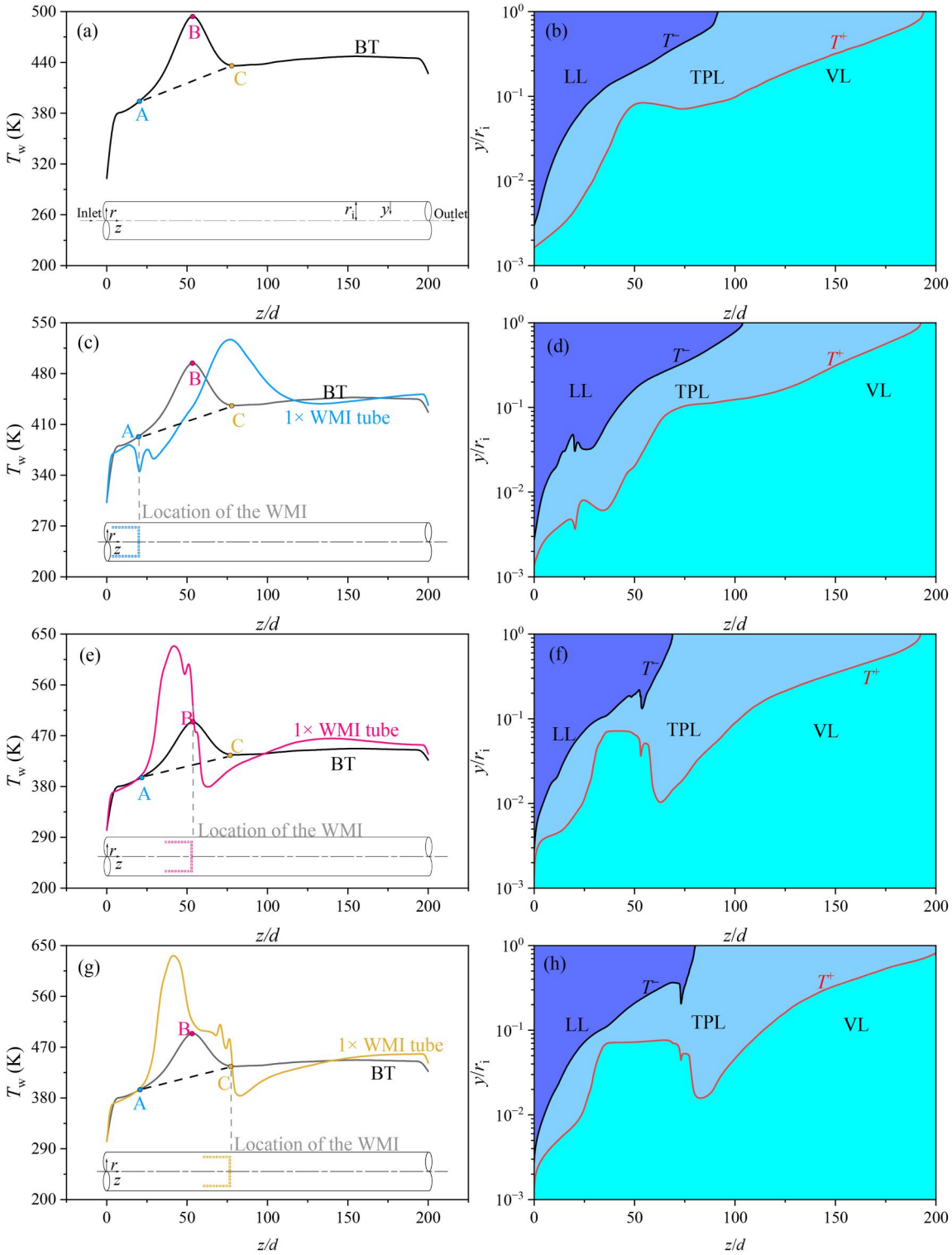


FIG. 8. Effects of wire-mesh location on the axial distributions of the inner-wall temperature and the pseudo-boiling phase partition. Panels (a)–(b) show the baseline BT; panels (c), (e), and (g) present T_w vs z/d for different insert locations (compared with BT), with the insert position indicated; panels (d), (f), and (h) show the corresponding pseudo-boiling phase diagrams, highlighting the axial distributions of the LL, TPL, and VL regions [$p = 8$ MPa, $G = 1000$ kg/(m^2 s), and $q = 210$ kW/m^2].

10 October 2026 07:25:36

Published under an exclusive license by AIP Publishing

is moved downstream by the insert. In contrast, when the wire mesh is placed near the wall temperature peak (point B, $z/d = 53$) or near the end of HTD (point C, $z/d = 77$), heat transfer is even further deteriorated compared with that in the bare tube, e.g., point A to point B in Fig. 8(e) and point A to point C in Fig. 8(g), and the peak wall temperature increases to 629 and 632 K, respectively, both much higher than that of the BT.

The pseudo-boiling phase diagrams further clarify the mechanism behind these differences. The phase diagram of the BT [Fig. 8(b)] shows that the near-wall VL region expands rapidly from point A to point B and forms a relatively thick VL layer. This high-thermal-resistance layer persists over a certain area, causing wall temperature overshoot and heat transfer deterioration. When the insert is positioned at point A [Fig. 8(d)], the disturbance and radial mixing induced by the wire mesh can delay or weaken the formation of the near-wall VL region, thereby reducing the VL layer thickness and suppressing wall temperature overshoot. In the cases of the insert positioned at $z/d = 53$ and $z/d = 77$ [Figs. 8(f) and 8(h)], the near-wall VL layer has already formed and developed upstream of the insert. Moreover, the wire mesh blocks the main flow somewhat, which even further thickens the near-wall VL layer. Although the local disturbance near the insert top can reconstruct the phase distribution to some extent, it cannot effectively suppress the already established high-thermal-resistance layer. Meanwhile, in the downstream region where fluid properties vary sharply, the VL region continues to grow. As a result, HTD is not well suppressed in the cases of the insert positioned at point B ($z/d = 53$) and point C ($z/d = 77$).

B. Effect of the number of wire-mesh inserts on HTD suppression

Based on the above finding that a single wire-mesh insert can effectively mitigate HTD and push the HTD region downstream when it is placed in front of the HTD onset (point A), it is interesting to examine the idea to use multiple inserts to completely suppress HTD throughout the heat transfer tube. Figure 9 compares the inner-wall temperature, T_w, between the BT and tubes with one, two, and three wire-mesh inserts, as well as the corresponding pseudo-boiling phase diagram.

As shown in Figs. 9(a), 9(c), and 9(e), increasing the number of inserts from one to three progressively reduces the peak T_w and shifts the peak location downstream. Specifically, the peak wall temperature decreases from 527 K (single insert) to 473 K (two inserts) and further to 462 K (three inserts). The peak T_w in the tube with two inserts is already lower than that of the BT. Compared with the single-insert case, multiple inserts achieve more continuous suppression downstream, maintaining lower T_w over a larger region. This is because the multiple inserts disturb the flow repeatedly, and enlarge its influenced region downstream.

The pseudo-boiling phase diagrams provide further insight into the underlying mechanism, as shown in Figs. 9(b), 9(d), and 9(f). The insert clearly affects the phase diagram. Specifically, the insert could decrease the VL thickness nearby the insert. With more inserts, the VL region is repeatedly thinned, while the TPL region gets closer to the wall. Thus, the evolution of the VL film toward downstream is strongly suppressed, and then heat transfer deterioration is mitigated.

These results suggest that multiple inserts introduce consecutive disturbances downstream of the HTD onset. Thus, the evolution of the VL film toward downstream is strongly suppressed, and then heat transfer deterioration is mitigated, reducing the wall-temperature overshoot. Compared with a single insert, the multiple inserts more effectively inhibit VL growth, and then have a larger region of thin VL film along the tube. This finding directly supports the subsequent design of periodic wire-mesh configurations by arranging inserts in the bare tube periodically, in which the near-wall VL film can be compressed over a longer axial distance, further weakening and even eliminating HTD.

C. HTD suppression by the periodic wire-mesh insert tube and the underlying mechanism

Based on the above findings, a PWMIT was further designed. To cover a wide range of operating conditions and avoid HTD occurring very close to the tube inlet, the first insert was fixed at the location of $z/d = 5$, and a total of ten inserts were installed. This configuration aims to completely suppress HTD of sCO_2 throughout the tube.

As shown in Fig. 10(a), the peak wall temperature in PWMIT is markedly reduced to 396 K, which is 91 K lower than that in BT. Meanwhile, T_w exhibits a periodic fluctuation behavior corresponding to the periodic arrangement of the wire-mesh insert, and the wall temperature in PWMIT remains consistently below that in BT, achieving heat transfer enhancement and HTD suppression throughout the tube. In contrast, the bulk temperature, T_b, presents nearly linear variation along the tube, and its difference between BT and PWMIT is small. This suggests that the periodic inserts have a limited influence on the mainstream thermal state. Their primary effect is concentrated on regulating near-wall transport and mitigating HTD by improving near-wall heat transfer rather than by substantially altering the overall heat input or the bulk heating process.

To quantify the suppression effect of the wire-mesh inserts on HTD in supercritical CO_2, Fig. 10(b) compares the streamwise distribution of the supercritical K number for the BT and the PWMIT. Following the definition in Ref. 33, the K number reflects the relative magnitude of the vaporization-induced momentum effect to the fluid inertia acting on the wall-adjacent VL film. A large K indicates a thick VL film with strong interfacial fluctuations, which is more prone to triggering HTD and wall-temperature overshoot. Conversely, a small K corresponds to a thinner and smoother VL film, benefiting for heat transfer. The K number is defined as

$$K = \left(\frac{q_w}{G\Delta i}\right)^2 \frac{\rho_{T^-}}{\rho_{T_w}}, \tag{11}$$

where Δi is the pseudo-boiling enthalpy rise, and ρ_{T^-} and ρ_{T_w} are the fluid densities evaluated at T^- and at the wall temperature T_w, respectively.

As shown in Fig. 10(b), K in PWMIT remains significantly lower than that in BT over the entire tube, and the high-K peaks associated with HTD in BT are strongly suppressed. This confirms that the periodic wire-mesh configuration effectively weakens the tendency of the near-wall VL film to thicken, preventing the high-thermal-resistance layer from developing in a sustained manner. In other words, by continuously interrupting the formation, growth, and development of the near-wall VL film along the tube, PWMIT converts the originally concentrated HTD behavior into a low-amplitude, controllable periodic response, thereby improving the overall heat transfer performance.

10 October 2026 07:25:36

Published under an exclusive license by AIP Publishing

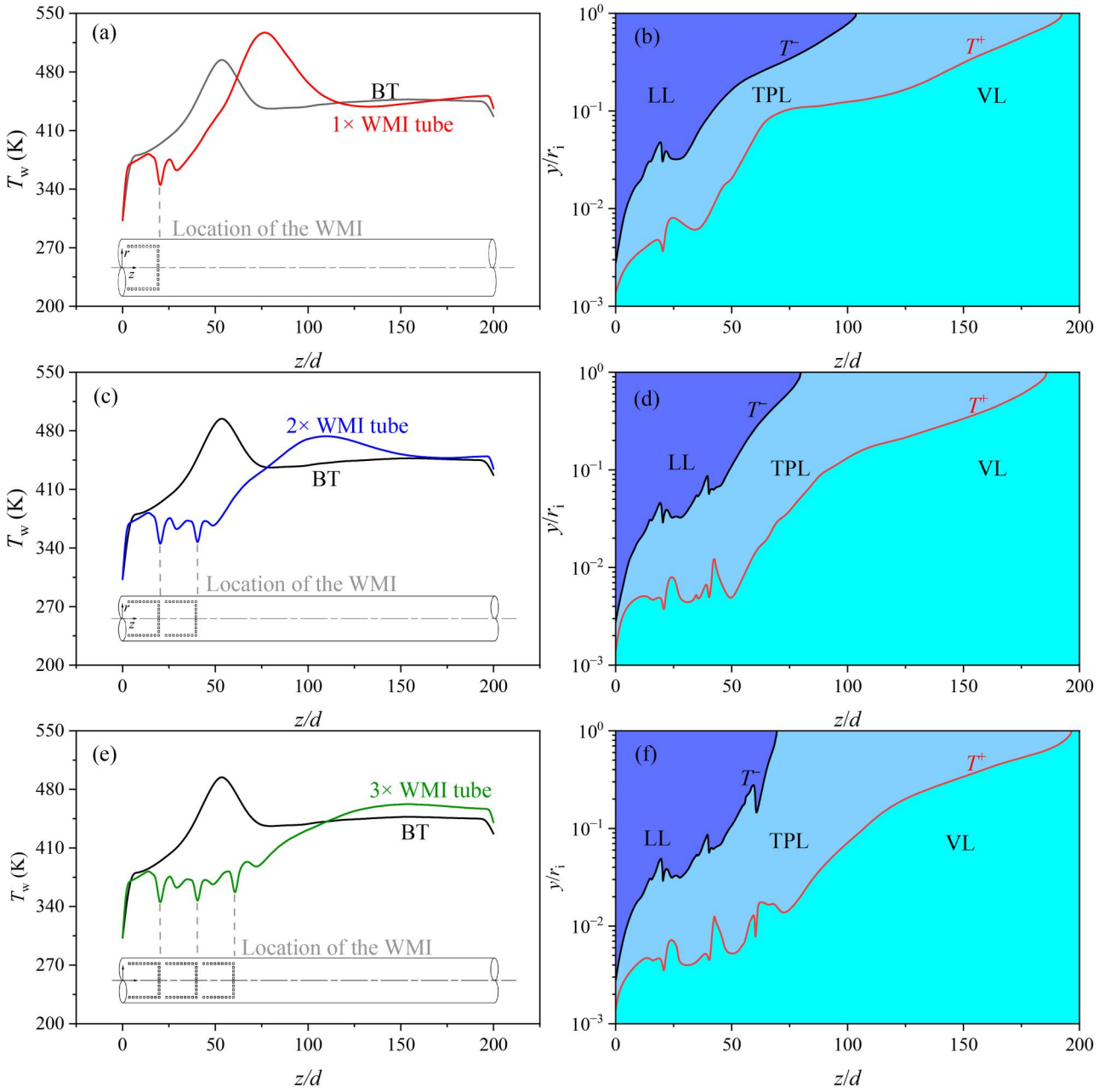


FIG. 9. Effects of the number of wire-mesh inserts on the axial distribution of the inner-wall temperature and the pseudo-boiling phase partition. (a), (c), and (e) show T_w vs z/d for tubes with one, two, and three wire-mesh inserts (WMIT), respectively, compared with BT, with the insert locations indicated. (b), (d), and (f) present the corresponding pseudo-boiling phase diagrams, showing the axial distributions of the LL, TPL, and VL regions [$p = 8$ MPa, $G = 1000$ kg/(m^2 s), and $q = 210$ kW/m^2].

The pseudo-boiling phase diagrams further clarify the suppression mechanism and corroborate the K-number analysis from the perspective of phase distribution characteristics. Compared with BT [Fig. 10(c)], the near-wall VL region in PWMIT [Fig. 10(d)] is clearly thinner, and its interface shows a periodic axial undulation. This implies that the near-wall VL film is periodically compressed by the periodic inserts, and its development is repeatedly interrupted. Meanwhile, the periodic inserts push the TPL region closer to the wall, indicating that more fluid accumulates near the wall. As a result, the near-wall thermal resistance is reduced, which suppresses the abnormal rise of T_w.

To further elucidate the local suppression mechanism of HTD by periodic wire-mesh inserts, Fig. 11 presents the local phase diagrams coupled with streamlines for BT and PWMIT in the section

10 October 2026 07:25:36

Published under an exclusive license by AIP Publishing

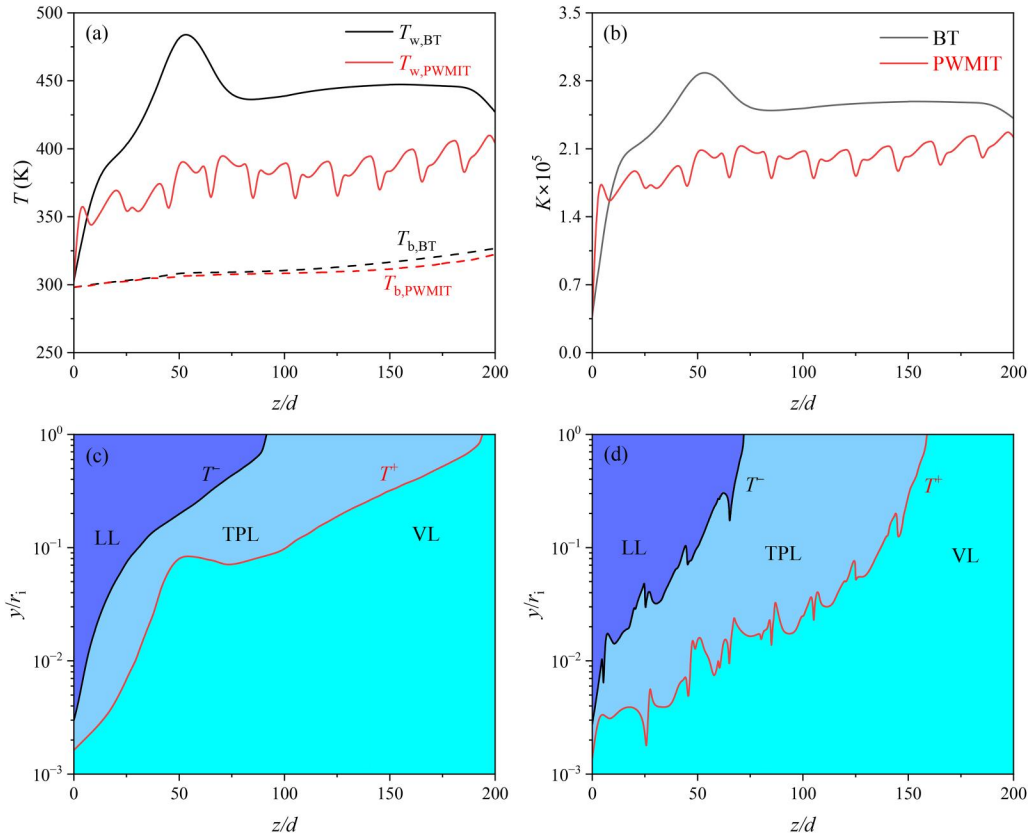


FIG. 10. HTD suppression by the periodic wire-mesh insert tube (PWMIT) and the associated state evolution. (a) Axial profiles of the wall temperature, T_w, and bulk temperature, T_b, vs z/d for BT and PWMIT; (b) axial distributions of the K number; (c) pseudo-boiling phase diagram for BT; and (d) pseudo-boiling phase diagram for PWMIT [$p = 8$ MPa, $G = 1000$ kg/(m^2 s), and $q = 210$ kW/m^2].

$z/d = 64.5$–65.5, a representative region around a typical wire-mesh unit. This allows direct observation of how the insert alters the near-wall phase distribution and the local flow structure. As shown in Fig. 11(a), BT exhibits a relatively regular phase distribution in this region. A clear radial stratification of LL–TPL–VL layers develops from the core toward the wall, and the near-wall VL region remains nearly uniform and flat. This indicates that the high-temperature and low-density VL layer adjacent to the wall can persist in a stable manner. Under such conditions, lateral disturbances across the VL film are weak, and the VL layer induces a high thermal resistance which hinders heat transport from the wall to the mainstream.

In contrast, Fig. 11(b) shows that the wire-mesh insert in PWMIT substantially modifies both the local flow and the phase structure. The streamlines deflect markedly near the top surface of the insert, suggesting a sustainable perturbation to the mainstream. As a result, the originally flat near-wall phase interfaces become locally curved and compressed, indicating that the insert interrupts the continuous growth of the near-wall VL layer and then reduces the layer thickness. Near the insert top, fluid is redistributed from the core toward the wall, enhancing the supply of cold fluid to the near-wall region. This weakens the near-wall VL film and improves the local heat transfer.

Figure 12 compares the axial variations of the heat transfer coefficient, h, and pressure, p, between BT and PWMIT. It is seen that PWMIT has a higher h than BT over the entire tube [see Fig. 12(a)]. In BT, h drops rapidly in the region where the wall temperature reaches peaks and then remains steadily low over a long downstream distance. This behavior is consistent with the near-wall VL film characteristics as discussed previously. In comparison, PWMIT presents much higher heat transfer coefficients which fluctuate periodically corresponding to the periodic inserts.

Figure 12(b) compares the pressure variation along the flow in BT and PWMIT. The pressure was obtained by taking cross sections at different axial locations along the flow direction and performing an area-integral average of the pressure over the fluid region of each cross section. The pressure in BT decreases smoothly along the tube, whereas PWMIT shows a large overall pressure drop with a stepwise pattern because of each insert. Therefore, PWMIT achieves enhanced heat transfer and HTD suppression, but with a penalty of pressure drop. It is then necessary to evaluate the comprehensive performance of the PWMIT to see the trade-off between heat transfer and pressure drop.

D. Effect of mass flux on the performance of PWMIT

To quantitatively evaluate the influence of the wire-mesh inserts on the flow and heat transfer of supercritical CO_2, the heat-transfer

10 October 2026 07:25:36

Published under an exclusive license by AIP Publishing

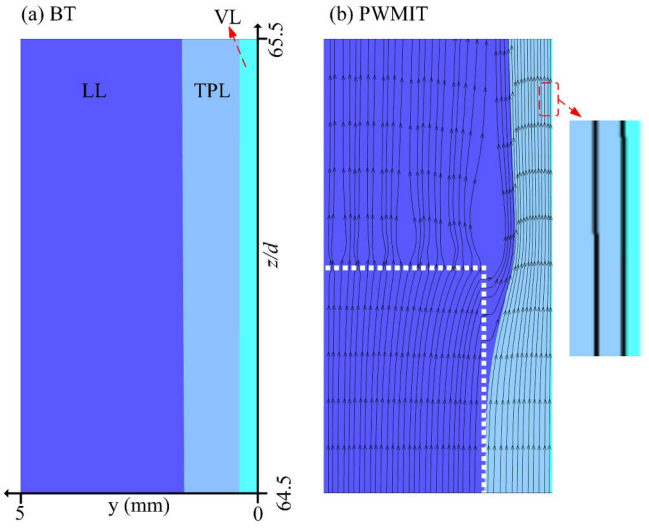


FIG. 11. Comparison of the local pseudo-boiling phase partition and flow structure around $z/d \approx 65$ for BT and PWMIT. (a) Phase partition in BT (LL, TPL, and VL) and (b) phase partition in PWMIT with streamlines [$p = 8$ MPa, $G = 1000$ kg/(m^2 s), and $q = 210$ kW/m^2].

enhancement factor (*EF*) and the overall performance evaluation criterion (*PEC*) are adopted as assessment metrics. The heat-transfer enhancement factor is defined as

$$EF = \frac{h}{h_0}, \tag{12}$$

where h and h_0 are the convective heat transfer coefficients in the PWMIT and the BT, respectively.

The *PEC* is commonly used to provide a comprehensive assessment of heat transfer and hydraulic performance. The present study uses the *PEC* defined in Ref. 58,

$$PEC = \frac{Nu/Nu_0}{(f/f_0)^{1/6}} = \frac{h/h_0}{(\Delta p/\Delta p_0)^{1/6}}, \tag{13}$$

where Δp and Δp_0 are the pressure drop of PWMIT and the BT, respectively. A value of $PEC > 1$ indicates that the benefit of heat transfer enhancement prevails over the penalty of pressure drop.

Figure 13 illustrates the effect of mass flux on *EF* and *PEC* at $p = 8$ MPa and $q = 170$ kW/m^2. As shown in Fig. 13(a), with increasing G, *EF* generally increases first and then decreases, accompanied by certain local fluctuations, and reaches its maximum near $G = 1000$ kg/m^2 s. At low G, the wire-mesh inserts have a limited effect on promoting near-wall fluid renewal and radial mixing, and thus the heat transfer enhancement is relatively weak. As G increases, the disturbance induced by the inserts is strengthened, the near-wall VL layer is compressed and its continuous development is suppressed, and the near-wall high-thermal-resistance layer becomes thinner, leading to a marked increase in *EF*. When G is further increased, the mainstream momentum and the inherent heat transfer capability of the bare tube are enhanced. As a result, the relative enhancement provided by the wire-mesh inserts becomes weaker, and *EF* generally decreases.

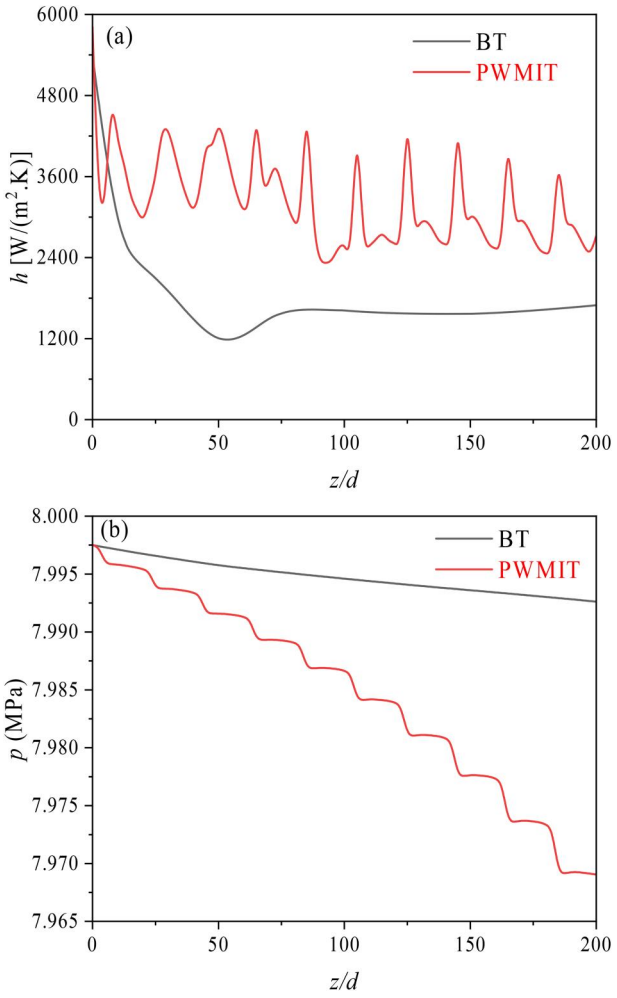


FIG. 12. Effects of the PWMIT on heat transfer and pressure drop, compared with BT. (a) Axial distribution of the heat transfer coefficient, h, vs z/d and (b) axial distribution of pressure, p, vs z/d [$p = 8$ MPa, $G = 1000$ kg/(m^2 s), and $q = 210$ kW/m^2].

As shown in Fig. 13(b), the variation of *PEC* with G is generally consistent with that of *EF*, while it is also affected by the pressure-drop penalty. At low mass flux, although the inserts can enhance heat transfer, the associated pressure-drop penalty is relatively significant, resulting in $PEC < 1$. As G increases, the heat transfer benefit gradually outweighs the pressure-drop penalty, and *PEC* increases to its maximum near $G = 1000$ kg/m^2 s. With a further increase in G, the heat transfer enhancement gradually weakens, whereas the additional pressure drop still exists. Therefore, *PEC* generally decreases and falls below 1 again at very high mass flux.

Overall, mass flux has a significant influence on the comprehensive performance of PWMIT. $PEC = 1$ represents the balance between the heat transfer benefit and the pressure-drop penalty, rather than a necessary asymptotic limit. Both excessively low and excessively high mass fluxes are unfavorable for comprehensive performance improvement. In contrast, an intermediate mass-flux range provides a better

10 October 2026 07:25:36

Published under an exclusive license by AIP Publishing

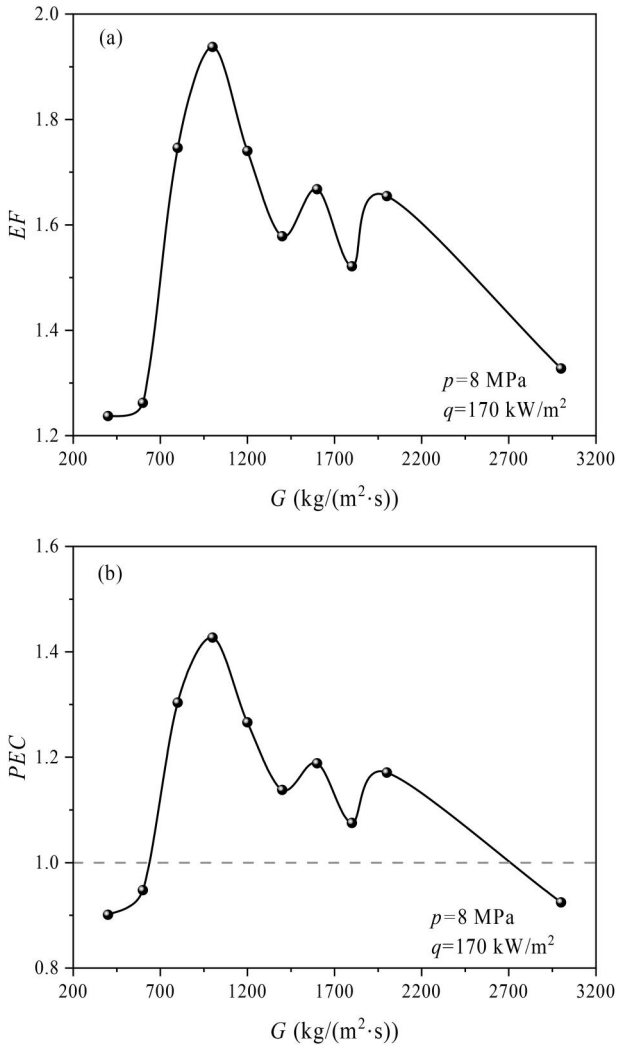


FIG. 13. Effect of mass flux, G, on the overall performance ($p = 8$ MPa and $q = 170$ kW/m^2). (a) Variation of the enhancement factor, *EF*, with G and (b) variation of the performance evaluation criterion, *PEC*, with G. The dashed line denotes $PEC = 1$.

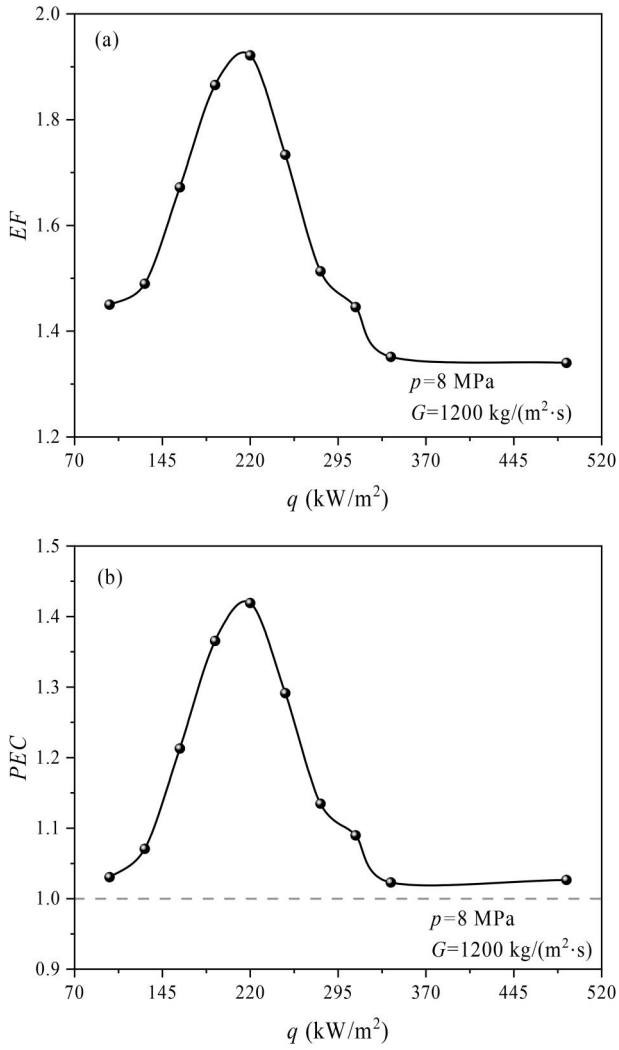


FIG. 14. Effect of heat flux, q, on the overall performance [$p = 8$ MPa and $G = 1200$ kg/(m^2 s)]. (a) Variation of the enhancement factor, *EF*, with q and (b) variation of the performance evaluation criterion, *PEC*, with q. The dashed line denotes $PEC = 1$.

balance among HTD suppression, heat transfer enhancement, and pressure-drop penalty.

E. Effect of heat flux on the performance of PWMIT

In addition to mass flux, the effect of heat flux on the performance of PWMIT was also examined. Figure 14 shows the effects of heat flux q on *EF* and *PEC* at $p = 8$ MPa and $G = 1200$ kg/m^2 s. As shown in Fig. 14(a), *EF* generally increases first and then decreases with increasing q, reaching its maximum near $q = 220$ kW/m^2. When q is lower than 220 kW/m^2, the near-wall VL layer in the bare tube becomes easier to develop and induce HTD as the heat flux increases. Under this condition, the wire-mesh inserts can enhance radial mixing and suppress the development of the near-wall VL layer, thereby strengthening heat transfer and increasing *EF*. When q is further increased beyond 220 kW/m^2, the relative heat transfer enhancement of PWMIT gradually weakens, and *EF* decreases accordingly and tends to level off at high heat flux.

As shown in Fig. 14(b), *PEC* follows a trend similar to that of *EF*, increasing first and then decreasing, with the peak also appearing near $q = 220$ kW/m^2. At low heat flux, HTD is not fully developed, and the heat transfer benefit provided by the wire-mesh inserts is limited; therefore, *PEC* approaches 1. As q increases, the heat transfer benefit becomes stronger and outweighs the pressure-drop penalty, leading to a marked increase in *PEC*. When q is further increased, the near-wall high-thermal-resistance layer becomes more pronounced, and the relative suppression capability of the wire-mesh inserts weakens. As a result, *PEC* gradually decreases and approaches 1 again at high heat flux. It should be noted that $G = 1200$ kg/m^2 s lies within a

10 October 2026 07:25:36

Published under an exclusive license by AIP Publishing

favorable mass-flux range for PWMIT. Therefore, even at low or high heat flux, *PEC* remains slightly higher than 1, indicating that the heat transfer benefit is almost balanced with the pressure-drop penalty. Overall, an intermediate heat-flux range enables PWMIT to achieve better comprehensive performance.

F. HTD suppression under different G–q combinations

The analysis above indicates that mass flux and heat flux influence the performance of PWMIT. It is then interesting to investigate the mass flux–heat flux combinations to enhance heat transfer and suppress HTD. Figure 15 summarizes a map that distinguishes effective and weak HTD suppression against the mass flux and heat flux. In the effective suppression, heat transfer is enhanced throughout the whole tube by the inserts and HTD is completely mitigated, while in the weak suppression, PWMIT still lowers the wall temperature but the HTD-like deterioration feature persists. It is seen that a large mass flux allows a large range of heat flux to have effective HTD suppression. The dashed line in Fig. 15 can be regarded as a boundary separating the two regimes of effective HTD suppression and weak HTD suppression. This transition boundary could be used to guide the design of working conditions, ensuring effective HTD suppression.

Figure 15 also helps explain the relative decreases in *EF* and *PEC* at several operating points in Figs. 13 and 14. For example, the cases of $G = 600\,\mathrm{kg/(m^2\,s)}$ and $q = 170\,\mathrm{kW/m^2}$ in Fig. 13 and $G = 1200\,\mathrm{kg/(m^2\,s)}$ and $q = 250\,\mathrm{kW/m^2}$ in Fig. 14 fall into the weak-suppression regime. Under these conditions, although PWMIT still improves heat transfer and lowers the wall temperature to some extent, HTD is not fully suppressed and the deterioration zone remains. As a result, the relative enhancement benefit becomes smaller than that in neighboring effective-suppression cases, leading to lower EF and PEC. This does not imply that the inserts become ineffective; rather, it indicates that the operating conditions deviate from the optimal HTD-suppression window.

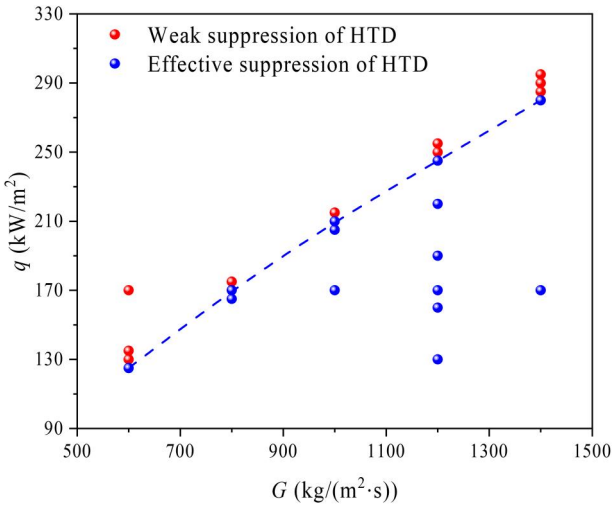


FIG. 15. Discrimination map of HTD suppression by PWMIT under different combinations of mass flux, *G*, and heat flux, *q*. Red circles denote weak suppression and blue circles denote effective suppression; the dashed line indicates the empirical boundary separating the two regimes.

IV. CONCLUSIONS

This study numerically investigates the flow and heat transfer of sCO_2 flow in a vertical tube. The pressure p is fixed at 8 MPa, with mass flux G ranging from 400 to 3000 $\mathrm{kg/(m^2\,s)}$ and heat flux q ranging from 100 to 490 $\mathrm{kW/m^2}$. Wire-mesh inserts are proposed to enhance sCO_2 heat transfer and suppress heat transfer deterioration (HTD) due to sharp variation of fluid properties. Based on the pseudo-boiling theory, the mechanisms and key factors associated with HTD are analyzed. The main conclusions are summarized as follows:

(1) The 2D numerical model could well predict the heat transfer behavior of sCO_2 in both NHT and HTD conditions, showing good agreement with experimental measurements.
(2) The location of a single wire-mesh insert strongly affects HTD suppression. A noticeable suppression is observed only when the insert is placed upstream of the HTD onset.
(3) Using multiple inserts produce consecutive disturbances which progressively reduce the peak wall temperature and compress the near-wall vapor-like (VL) film. This inhibits downstream VL regrowth, and provides a more stable HTD suppression.
(4) A periodic wire-mesh insert tube (PWMIT) is proposed, which can suppress HTD throughout the whole tube. Compared with a bare tube, PWMIT exhibits a much lower peak wall temperature and a significantly thinned near-wall VL film. These features indicate that PWMIT suppresses the formation and persistence of the near-wall high-thermal-resistance layer by periodically promoting near-wall fluid renewal and radial mixing.
(5) The heat-transfer enhancement factor and the performance evaluation criterion increase first and then decrease with either G or q in PWMIT. The G–q map further classifies PWMIT performance into effective suppression and weak suppression, which provide guidance for both configuration deployment and operating-condition selection.
(6) The present work is mainly a mechanism-oriented numerical study of PWMIT for suppressing heat transfer deterioration of supercritical CO_2. The results reveal the suppression mechanism and provide guidance for future experiments and structural optimization, including wire-mesh parameters, insert number, arrangement location, and applicable operating conditions. Future work will include direct experimental validation and further assessment of structural reliability and engineering applicability.

ACKNOWLEDGMENTS

The authors acknowledge the support from National Natural Science Foundation of China (Grant No. 52130608) and the Fundamental Research Funds for the Central Universities (2026TX006 and 2020DF002).

AUTHOR DECLARATIONS

Conflict of Interest

The authors have no conflicts to disclose.

Author Contributions

Qiuru Dong and Zhen Cao contributed equally to this work.

10 October 2026 07:25:36

Published under an exclusive license by AIP Publishing

Qiuru Dong: Formal analysis (equal); Investigation (lead); Visualization (lead); Writing – original draft (equal). **Zhen Cao:** Formal analysis (equal); Methodology (lead); Software (lead); Writing – original draft (equal). **Jian Xie:** Conceptualization (lead); Project administration (lead); Writing – review & editing (lead). **Jinliang Xu:** Funding acquisition (lead); Resources (lead); Supervision (lead). **Xin Wang:** Data curation (lead); Visualization (supporting). **Jing Tang:** Validation (lead); Visualization (supporting).

DATA AVAILABILITY

The data that support the findings of this study are available from the corresponding author upon reasonable request.

NOMENCLATURE

A	Flow-through area of 3D apertures (m^2)
A'	Flow-through area of 2D apertures (m^2)
D	Tube inner diameter (mm)
D_e	Equivalent diameter of 3D apertures (m)
D'_e	Equivalent diameter of 2D apertures (m)
D_m	Diameter of the wire-mesh (mm)
EF	Heat-transfer enhancement factor (–)
G	Mass flux [kg/(m^2 s)]
h	Heat transfer coefficient (W/m^2 K)
i_{pc}	Specific enthalpy at T_{pc} (J/kg)
L_b	Axial pitch/spacing between sleeves (mm)
L_m	Length of the wire-mesh sleeve (mm)
P	Operating pressure (MPa)
PEC	Performance evaluation criterion (–)
q	Heat flux (W/m^2)
T	Temperature (K)
T_b	Bulk mixed-mean temperature (K)
T_{pc}	Pseudocritical temperature (K)
T_w	Wall temperature (K)
T^-	Pseudo-boiling start temperature (K)
T^+	Pseudo-boiling end temperature (K)
w	Square-aperture width (3D) (μm)
w'	Slit width (2D) (μm)
Δi	Pseudo-boiling enthalpy rise (J/kg)
Δp	Pressure drop (Pa)
Δp_0	Pressure drop of bare tube (Pa)

Greek symbols

δ	Wire diameter of the 3D wire mesh (μm)
δ'	Equivalent wire diameter (2D) (μm)
λ	Thermal conductivity [W/(m K)]
μ	Dynamic viscosity (Pa s)
ρ	Density (kg/m^3)

Subscripts

b	Bulk
pc	Pseudocritical
w	Wall
0	Bare-tube/reference case

Abbreviations

BT	Bare tube
HTD	Heat transfer deterioration
LL	Liquid-like
NHT	Normal heat transfer
PWMIT	Periodic wire-mesh inserted tube
sCO_2	Supercritical carbon dioxide
TPL	Two-phase-like
VL	Vapor-like
WMIT	Wire-mesh-inserted tube

REFERENCES

[1]G. Liao, L. Liu, J. E. F. Zhang, J. Chen *et al.*, "Effects of technical progress on performance and application of supercritical carbon dioxide power cycle: A review," Energy Convers. Manage. **199**, 111986 (2019).

[2]M. Li, X. Zhang, Y. Xu, N. Liu, and W. Zhang, "Development and applications of supercritical CO_2 power cycles in nuclear, solar and other energy industries," Appl. Therm. Eng. **126**, 255–275 (2017).

[3]Y. Fan, G. Tang, X. Li, and D. Yang, "General and unique issues at multiple scales for supercritical carbon dioxide power system: A review on recent advances," Energy Convers. Manage. **268**, 115993 (2022).

[4]S. Guo, X. Guo, G. Wang, Y. Guo, Z. Wang *et al.*, "Conceptual design of a novel megawatt portable nuclear power system by supercritical carbon dioxide Brayton cycle coupled with heat pipe cooled reactor," Int. J. Adv. Nucl. React. Des. Technol. **5**, 168–188 (2023).

[5]X. Wang, Q. Liu, and Z. Bai, "Thermodynamic analysis of the cascaded supercritical carbon dioxide cycle integrated with solar and biomass energy," Energy Procedia **105**, 445–452 (2017).

[6]Y. Le Moullec, "Conceptual study of a high efficiency coal-fired power plant with CO_2 capture using a supercritical CO_2 Brayton cycle," Energy **49**, 32–46 (2013).

[7]Y. Feng, J. Qu, Y. Gao, Y. Zhu, and J. Shi, "Configuration design and performance optimization of a hybrid power system integrating multi-stack solid oxide fuel cell and supercritical carbon dioxide Brayton cycle with thermal energy storage," J. Energy Storage **131**, 117499 (2025).

[8]J. Lv, Y. Sun, C. Yuan, T. Qin, W. Ding *et al.*, "Thermal analysis and performance optimization of supercritical carbon dioxide Brayton cycle based on ship waste heat," Int. J. Heat Fluid Flow **117**, 110020 (2026).

[9]S. Li, Y. Song, T. Chang, Q. Yu, Y. Zhang *et al.*, "Revolutionizing 300 °C industrial steam with a novel transcritical carbon dioxide heat pump system: Thermodynamic and configuration analyses," Energy Convers. Manage. **346**, 120556 (2025).

[10]J. Lian, D. Xu, H. Chang, Z. Xu, X. Lu *et al.*, "Thermal and mechanical performance of a hybrid printed circuit heat exchanger used for supercritical carbon dioxide Brayton cycle," Energy Convers. Manage. **245**, 114573 (2021).

[11]F. Zhang, F. Lei, M. Feng, G. Liao, and J. E, "Investigation on the effect of the cooler design on the performance of onboard supercritical carbon dioxide power cycle for hypersonic vehicles," Appl. Therm. Eng. **236**, 121854 (2024).

[12]J. Xie and G. Xie, "Three-dimensional wake transition for CO_2 flow at supercritical pressure over single heated cylinder," Phys. Fluids **34**, 094106 (2022).

[13]D. Ma, X. Wang, S. Yang, and X. Shen, "Heat-transfer and stress-strain analyses of solar receiver with supercritical carbon dioxide as heat transfer fluid," Energy **324**, 136006 (2025).

[14]B. Yu, J. Xie, J. Xu, Q. Dong, and L. Cheng, "Pseudo-boiling of supercritical CO_2 in horizontal tubes: The influence of tube diameter," Phys. Fluids **37**, 073324 (2025).

[15]J. Xie, D. Liu, H. Yan, G. Xie, and S. K. S. Boetcher, "A review of heat transfer deterioration of supercritical carbon dioxide flowing in vertical tubes: Heat transfer behaviors, identification methods, critical heat fluxes, and heat transfer correlations," Int. J. Heat Mass Transfer **149**, 119233 (2020).

[16]J. D. Jackson, "Fluid flow and convective heat transfer to fluids at supercritical pressure," Nucl. Eng. Des. **264**, 24–40 (2013).

10 October 2026 07:25:36

Published under an exclusive license by AIP Publishing

[17]F. Sun, Y. Li, O. Manca, and G. Xie, "An evaluation on the laminar effect of buoyancy-driven supercritical hydrocarbon fuel flow and heat transfer characteristics," Int. J. Heat Mass Transfer **142**, 118414 (2019).
[18]D. M. McEligot and J. D. Jackson, ""Deterioration" criteria for convective heat transfer in gas flow through non-circular ducts," Nucl. Eng. Des. **232**, 327–333 (2004).
[19]S. Liu, Y. Huang, G. Liu, J. Wang, and L. K. H. Leung, "Improvement of buoyancy and acceleration parameters for forced and mixed convective heat transfer to supercritical fluids flowing in vertical tubes," Int. J. Heat Mass Transfer **106**, 1144–1156 (2017).
[20]D. E. Kim and M. H. Kim, "Experimental study of the effects of flow acceleration and buoyancy on heat transfer in a supercritical fluid flow in a circular tube," Nucl. Eng. Des. **240**, 3336–3349 (2010).
[21]Y. Jin, P. Zhao, M. Lei, and Y. Wan, "Influence of buoyancy on turbulence and heat transfer of supercritical CO_2 in vertical backward-facing step flows," Phys. Fluids **37**, 025169 (2025).
[22]B. Zhu, J. Xu, H. Zhang, J. Xie, and M. Li, "Effect of non-uniform heating on $scCO_2$ heat transfer deterioration," Appl. Therm. Eng. **181**, 115967 (2020).
[23]J. Xu, Y. Wang, and X. Ma, "Phase distribution including a bubblelike region in supercritical fluid," Phys. Rev. E **104**, 014142 (2021).
[24]X. He, J. Xu, X. Yu, and J. Xie, "Distinguishing evaporation-like and boiling-like modes of pseudo-boiling in supercritical pressures," Int. J. Heat Mass Transfer **214**, 124417 (2023).
[25]F. Maxim, C. Contescu, P. Boillat, B. Niceno, K. Karalis *et al.*, "Visualization of supercritical water pseudo-boiling at Widom line crossover," Nat. Commun. **10**, 4114 (2019).
[26]X. He, J. Xu, and J. Xie, "Quantitative characterization of the pseudo-boiling contribution to supercritical heat transfer," Phys. Fluids **36**, 013343 (2024).
[27]Y. Kanda, H. Ito, L. Chen, and A. Komiya, "Optical visualization of heat transfer in supercritical carbon dioxide under near-critical, liquid-like, and gas-like conditions," Phys. Fluids **35**, 067108 (2023).
[28]G. G. Simeoni, T. Bryk, F. A. Gorelli, M. Krisch, G. Ruocco *et al.*, "The Widom line as the crossover between liquid-like and gas-like behaviour in supercritical fluids," Nat. Phys. **6**, 503–507 (2010).
[29]Q. Wang, X. Ma, J. Xu, M. Li, and Y. Wang, "The three-regime-model for pseudo-boiling in supercritical pressure," Int. J. Heat Mass Transfer **181**, 121875 (2021).
[30]N. L. Kafengauz and M. I. Fedorov, "Excitation of high-frequency pressure oscillations during heat exchange with diisopropylcyclohexane," J. Eng. Phys. **11**, 63–104 (1966).
[31]B. Zhu, J. Xu, X. Wu, J. Xie, and M. Li, "Supercritical "boiling" number, a new parameter to distinguish two regimes of carbon dioxide heat transfer in tubes," Int. J. Therm. Sci. **136**, 254–266 (2019).
[32]L. Cheng and J. Xu, "Experimental investigation of non-uniform heating effect on flow and heat transfer of supercritical carbon dioxide: An application to solar parabolic trough collector," Renewable Energy **236**, 121373 (2024).
[33]B. Yu, J. Xie, J. Xu, Q. Dong, and L. Cheng, "Numerical study on pseudo-boiling heat transfer of supercritical CO_2 in horizontal tube," Int. J. Heat Mass Transfer **244**, 126981 (2025).
[34]A. M. Dolatabadi, G. Petruccelli, A. Grönman, and T. Turunen-Saaresti, "Onset of heat transfer deterioration caused by the gas-like layer formation in horizontal tubes using supercritical CO2," Int. J. Heat Mass Transfer **261**, 128557 (2026).
[35]R. Xu, F. Luo, and P. Jiang, "Experimental research on the turbulent convection heat transfer of supercritical pressure CO_2 in a serpentine vertical mini tube," Int. J. Heat Mass Transfer **91**, 552–561 (2015).
[36]J. Xu and D. Sun, "Turbulent convective heat transfer of CO_2 in a helical tube at near-critical pressure," Int. J. Heat Mass Transfer **80**, 748–758 (2015).
[37]Y.-Y. Bae, H.-Y. Kim, and T. H. Yoo, "Effect of a helical wire on mixed convection heat transfer to carbon dioxide in a vertical circular tube at supercritical pressures," Int. J. Heat Fluid Flow **32**, 340–351 (2011).
[38]N. Yuan, D. Bi, Y. Zhai, Y. Jin, Z. Li *et al.*, "Flow and heat transfer performance of supercritical pressure carbon dioxide in pipes with discrete double inclined ribs," Int. J. Heat Mass Transfer **149**, 119175 (2020).
[39]S. Li, X. Liu, Y. Zeng, L. Li, C. He *et al.*, "Numerical study of dimpled structures on heat transfer deterioration mitigation with supercritical CO_2 heated in vertical tube," Appl. Therm. Eng. **259**, 124925 (2025).
[40]P. Xiang, J. Wang, Y. Wang, Z. Chen, Y. Kang *et al.*, "Mitigation effects of lattice structure arrays on the heat transfer deterioration of supercritical CO_2," Appl. Therm. Eng. **257**, 124171 (2024).
[41]J. Wang, P. Xiang, Y. Lei, B. Xu, Y. Zhang *et al.*, "Vortex-driven heat transfer enhancement in supercritical CO_2: Structural optimization with claw-shaped lattice design for enhanced thermal performance," Int. Commun. Heat Mass Transfer **167**, 109275 (2025).
[42]F. Xing, J. Xie, and J. Xu, "Modulated heat transfer tube with mesh cylinder inserted," Int. Commun. Heat Mass Transfer **56**, 15–24 (2014).
[43]Z. Cao, J. Xu, D. Sun, J. Xie, F. Xing *et al.*, "Numerical simulation of modulated heat transfer tube in laminar flow regime," Int. J. Therm. Sci. **75**, 171–183 (2014).
[44]R. Kurian, C. Balaji, and S. P. Venkateshan, "Experimental investigation of near compact wire mesh heat exchangers," Appl. Therm. Eng. **108**, 1158–1167 (2016).
[45]Y. Li, W. Li, J. Xie, J. Xu, and Z. Miao, "Eliminating flooding by phase separation in condenser tube," Phys. Fluids **34**, 123310 (2022).
[46]J. Xie, J. Xu, C. Liang, Q. She, and M. Li, "A comprehensive understanding of enhanced condensation heat transfer using phase separation concept," Energy **172**, 661–674 (2019).
[47]M. Liu, S. Liu, D. Xi, S. Huang, and Y. Huang, "Analysis of heat transfer mechanism in supercritical fluids from the aspect of pool heating," Front. Energy Res. **10**, 1042391 (2023).
[48]B. Zhu, Q. Zhang, L. Ma, and H. Shi, "Analysis of heat transfer deterioration mechanism of supercritical fluid based on VOF two-phase method and pseudo-boiling theory," Int. J. Heat Mass Transfer **240**, 126643 (2025).
[49]K. Wang, X. Xu, Y. Wu, C. Liu, C. Dang *et al.*, "Numerical investigation on heat transfer of supercritical CO_2 in heated helically coiled tubes," J. Supercrit. Fluids **99**, 112–120 (2015).
[50]X. Du, Z. Lv, S. Zhao, Q. Qiu, and X. Zhu, "Numerical analysis of diameter effects on convective supercritical water flow in a vertical round tube," Appl. Therm. Eng. **160**, 114095 (2019).
[51]Y. Li, F. Sun, G. Xie, B. Sunden, and J. Qin, "Numerical investigation on flow and thermal performance of supercritical CO_2 in horizontal cylindrically concaved tubes," Appl. Therm. Eng. **153**, 655–668 (2019).
[52]J. Wang, J. Yang, J. Gong, C. Zhao, and K. Hooman, "A designed wall roughness approach to improve turbulent heat transfer to supercritical CO_2 flowing in horizontal tubes," J. Supercrit. Fluids **190**, 110573 (2022).
[53]F. R. Menter, "Two-equation eddy-viscosity turbulence models for engineering applications," AIAA J. **32**, 1598–1605 (1994).
[54]ANSYS, Inc., *ANSYS Fluent Theory Guide, Release 19.2* (ANSYS, Inc., Canonsburg, PA, 2019).
[55]A. M. Dolatabadi, M. Zocca, G. Petruccelli, A. Grönman, and T. Turunen-Saaresti, "Guiding the optimization of the thermal-hydraulic performance of advanced-CSP systems integrated with thermal energy storage, considering the pseudo-boiling phenomenon," Energy **360**, 141628 (2026).
[56]C. Yan, J. Xu, B. Zhu, X. He, and G. Liu, "Numerical study on convective heat transfer of supercritical CO_2 in vertically upward and downward tubes," Sci. China: Technol. Sci. **64**, 995–1006 (2021).
[57]H. Cheng, J. Zhao, and M. K. Rowinski, "Study on two wall temperature peaks of supercritical fluid mixed convective heat transfer in circular tubes," Int. J. Heat Mass Transfer **113**, 257–267 (2017).
[58]X. Y. Zhang, Z. C. Liu, and W. Liu, "Numerical studies on heat transfer and flow characteristics for laminar flow in a tube with multiple regularly spaced twisted tapes," Int. J. Therm. Sci. **58**, 157–167 (2012).

10 October 2026 07:25:36

Published under an exclusive license by AIP Publishing